Geophys. J. Int. (2010) **181,** 198–220 doi: 10.1111/j.1365-246X.2010.04528.x

A multiphase model of core formation

Ondřej Šrámek,[1]* Yanick Ricard[2] and Fabien Dubuffet[2]

[1] *Department of Geophysics, Faculty of Mathematics and Physics, Charles University in Prague, V Holešovičkách* 2, 180 00 *Praha* 8, *Czech Republic. E-mail: ondrej.sramek@colorado.edu*

[2] *Laboratoire des Sciences de la Terre, CNRS, Université de Lyon* 1, *ENSL* 46 *allée d'Italie,* F-69364 *Lyon, Cedex* 07, *France*

Accepted 2010 January 19. Received 2010 January 8; in original form 2009 June 10

SUMMARY

The differentiation of solid planets with segregation of metal from silicates happens during the Hadean time while the planet is still growing by accretion. The separation of metal occurs when at least the metallic phase is liquid and proceeds by a combination of transport by diapiric instabilities and by more diffuse percolation flow. In this paper we develop a formalism derived from Bercovici *et al*. that can handle simultaneously two components, silicates and metal, and where the metal can be present both in solid and liquid states. The mechanical equations are non-Boussinesq as the lateral density variations are of the same order as the density itself. When the metal is solid, the metal and the silicates are locked together and we treat their mixture as a single-phase fluid where density is function of composition (iron–silicate proportions). When metal is liquid, it can separate from the silicates and the two phases interact through shear stress (e.g. Darcy flow) and normal stress. The evolution of the volume proportion of liquid iron is controlled by the difference of pressure between the solid and liquid phases. The energy conservation equation takes into account the different mechanisms by which the gravitational energy is dissipated as heat. The 2-D Cartesian numerical code that we implemented to solve these equations makes use of numerical techniques that have not been previously used in geophysical two-phase modelling; we discuss the numerical aspects and benchmark the solutions. We present simulations of core–mantle differentiation showing that the first impact that melts the iron phase near the surface is potentially able to trigger the whole core–mantle segregation in a runaway phenomenon. The threshold of this instability in terms of the impactor and planetary size and the initial planetary temperature is investigated. The segregation of the metal occurs by a mechanism that was not suggested before and which is intermediate between the usual diapir instability and a porosity wave. Although we cannot explore the whole parameter space of our numerical model, we show various simulations that clarify the role of the most important parameters, such as the solid and metal viscosities or the depth dependence of gravity.

Key words: Numerical solutions; Mantle processes; Impact phenomena; Planetary interiors.

1 INTRODUCTION

The Hadean time of the Earth during which the planet was simultaneously growing by accretion and ongoing core–mantle segregation is poorly understood. During a few millions years after condensation of the first solids in the solar nebula, the growing planetesimals were heated by the radioactive decays of isotopes that are now extinct such as ^{26}Al and ^{60}Fe (with half-lives of 0.73 and 1.5 Myr, respectively). Silicate–metal differentiation seems to have occurred within planetesimals at a time where these now extinct radioactivities were delivering their heat (Carlson & Langmuir 2000; Walter & Tronnes 2004). The chronology of core formation has been constrained by the ^{182}Hf–^{182}W parent–daughter system with a half-life of 9 Myr. Both are highly refractory but the hafnium is lithophile and the tungsten siderophile, so that core–mantle separation before 9 Myr generates an excess of radiogenic tungsten in the mantle. The Earth's mantle, with a slightly higher ^{182}W/^{183}W ratio than chondrites indicates a rapid core formation but probably delayed 30 Myr after the beginning of accretion (Kleine *et al.* 2002; Yin *et al.* 2002; Kleine *et al.* 2004). However, the complexities of the final accretion by large impacts make this estimate more uncertain than previously thought (Nimmo & Agnor 2006).

After the decay of the initial radioactivity, it is only when the proto-planets reach a radius of a thousand kilometres that their own

*Now at: University of Colorado at Boulder, Department of Physics, Boulder, CO, USA.

gravity becomes large enough to provide a new source of thermal energy (Senshu *et al.* 2002). When the impact velocities become larger than elastic velocities, the kinetic energy of impactors can be released at large depth in the impacted body by the induced shock wave (Tonks & Melosh 1993). Therefore, when an undifferentiated planet reaches a Mars size, the impacts can induce melting and one or more magma oceans can be formed, as was probably the case for the Earth (Benz & Cameron 1990; Greenwood *et al.* 2005). The blanketing presence of a thick atmosphere also favours the existence of magma oceans (Matsui & Abe 1986a).

If planets grow to their final sizes in a very short time, comparable to the half lives of ^{26}Al or ^{60}Fe, they can remain hot during all the accretion process, with impact heating overlapping with radioactive heating. However, as small size planetesimals cool rapidly (the cooling time of a 10-km-size planetesimal is only 1 Myr), the terrestrial planets possibly had a cooling period where they were growing with a moderate temperature by accretion of undifferentiated or differentiated planetesimals that had already lost their heat sources (Kaula 1979). Planets might therefore have undergone a two-stage heating history with a first period of radioactive heating and a few million years later a second period of surface heating. This period of surface heating culminated by large and stochastic impacts in the last stages of accretion (Canup & Asphaug 2001).

The scenario of magma oceans is supported by the abundances of moderately siderophile elements in Earth's mantle (Li & Agee 1996). In a magma ocean, the metal–silicate differentiation occurs rapidly (Rubie *et al.* 2003) and a layer of liquid metal (continuous or in the form of various metallic ponds) is formed at the interface between the deep undifferentiated and rather cold inner planet and the shallow hot silicate residue. Due to the rather large difference in melting temperature between silicates and metal (especially when the metal contains minor components that can decrease significantly its melting temperature; Boehler 1996), there is probably a significant time window during which shock heating is intense enough to melt the metallic phase but leaves the silicates in the solid phase. The resulting dense liquid metal layer is unstable and by a Rayleigh Taylor mechanism, can form one or numerous metallic diapirs that could sink through the undifferentiated core. The penetration of these mantle diapirs through a colder undifferentiated deeper planet is poorly understood. In the form of large diapirs, the Stokes sinking velocities appears much too slow (Honda *et al.* 1993). The penetration could be facilitated by the stress-dependent viscosity that should be associated with the large deviatoric stresses of these diapirs, by the release of potential energy increasing locally the temperature or by hydraulic fracture (Rushmer *et al.* 2000).

This qualitative scenario explains how an undifferentiated planet may evolve to an unstable stratified planet, where the temperature decreases with depth, with a shallow layer of silicates, overlying a liquid metallic shell, and a colder undifferentiated core. However, it is still very uncertain how after the sinking of the first metallic diapirs, the rest of the undifferentiated mantle is processed. Gerya & Yuen (2007) suggest that this may happen by a rapid translation of the undifferentiated mantle around the proto-core formed by the first diapir. The metal of the undifferentiated deep layers could separate by percolation. The topology of the metal phase sinking through the mantle (droplets, connected network or large diapirs) controls the chemical equilibrium or disequilibrium between the mantle and the core (Karato & Murthy 1997). The surface tension between metal and silicates does not favour the connectivity of the metallic phase at low metallic proportion, at least at low pressure (von Bargen & Waff 1986). However the proportion of metal was probably large enough that the metallic pores connected anyway, mostly at great depth where the effects of surface tension diminishes (Urakawa *et al.* 1987).

It is a formidable task to test all these complex fluid dynamics phenomena with realistic parameters. The Rayleigh numbers involved in these situations, range from very large to extremely high. If silicates are still in their solid phase, the Rayleigh number may not be much larger than in the present-day mantle. If silicates are melted, the Rayleigh might reach 10^{29} (Solomatov 2000). The lateral viscosity variations are huge, various phases are simultaneously present—potentially four phases, with iron and silicates both in their solid and liquid states, the convection is non-Boussinesq (as the density difference between metal and silicate is comparable to that of silicates) and self-gravitation should be accounted for (as gravity changes drastically during core segregation; see e.g. Gerya & Yuen 2007). All these characteristics explain why the numerical simulations have been up to now rather simple and have involved different aspects of diapir penetration (Honda *et al.* 1993; Gerya & Yuen 2007; Samuel & Tackley 2008; Monteux *et al.* 2009), droplet motions (Rubie *et al.* 2003) or advection of dense metallic tracers (Höink *et al.* 2006).

Following our recent results (Ricard *et al.* 2009), we propose a general modelling approach that uses a multiphase formalism that can handle the simultaneous presence of solid silicate, solid and liquid metal. We follow the results developed in Bercovici *et al.* (2001) and Bercovici & Ricard (2003). The equations are close to those proposed by McKenzie (1984) and used in various papers (e.g. Spiegelman & McKenzie 1987; Kelemen *et al.* 1997; Schmeling 2000; Šrámek *et al.* 2007; Katz 2008). It is however the first time they are applied with minimal approximation in a large-scale simulation of the core segregation.

Our model and some of the results were briefly described in an earlier paper (Ricard *et al.* 2009). Here we largely extend the presentation. We present the theoretical model in detail. The computational method is thoroughly discussed and particular detail is taken when describing the advection method for the porosity that has not been previously used in geodynamical two-phase modelling. Some benchmark calculations are included. Finally, we present various additional cases that were not incorporated into Ricard *et al.* (2009), and discuss the effect of model parameters on the segregation dynamics.

2 A MULTIPHASE FORMALISM

2.1 Two-phase equations: liquid metal and solid silicates

We first present the equations assuming that the metal phase is entirely fluid and the silicate phase entirely solid. Later in Section 2.3, we show that the more complex case where the metallic component can be present in both solid and liquid states can be handled with minor modifications. The two phases, metal and silicate, in volume proportions ϕ and $1-\phi$, have properties denoted by the subscripts f and m (fluid and matrix). Each phase is incompressible, therefore the densities ρ_f and ρ_m are constant. The mixture is itself incompressible and the continuity equation is

$$\nabla \cdot [\phi \mathbf{v}_f + (1-\phi)\mathbf{v}_m] = 0, \tag{1}$$

where $\mathbf{v}_f$ and $\mathbf{v}_m$ are the volume averaged metal and silicate velocities. The porosity change is related to the difference in velocities between the two phases, $\Delta\mathbf{v} = \mathbf{v}_m - \mathbf{v}_f$ and satisfies

$$\frac{\mathrm{D}\phi}{\mathrm{D}t} = \nabla \cdot [\phi(1-\phi)\Delta\mathbf{v}]. \tag{2}$$

The Lagrangian derivative includes the advection by the volume average mixture velocity $\overline{\mathbf{v}} = \phi\mathbf{v}_f + (1-\phi)\mathbf{v}_m$,

$$\frac{\mathrm{D}}{\mathrm{D}t} = \frac{\partial}{\partial t} + [\phi\mathbf{v}_f + (1-\phi)\mathbf{v}_m]\cdot\nabla; \tag{3}$$

we use a notation where volume average quantities are denoted with an overscript, for example, $\overline{\mathbf{v}} = \phi\mathbf{v}_f + (1-\phi)\mathbf{v}_m$, and difference quantities by a Δ, for example, $\mathbf{\Delta v} = \mathbf{v}_m - \mathbf{v}_f$.

The total momentum equation for the metal–silicate mixture in the infinite Prandtl number approximation (no inertial forces) is

$$-\nabla\overline{P} + \nabla\cdot[\mu^*\underline{\boldsymbol{\tau}}_m] + [\phi\rho_f + (1-\phi)\rho_m]\mathbf{g} = 0, \tag{4}$$

where $\mathbf{g}$ is gravitational acceleration and $\mu^* = 1-\phi$, assuming that the molten metal cannot hold deviatoric stresses because its viscosity is negligible with respect to that of solid silicates. We have neglected the surface tension term in eq. (4). The matrix stress tensor is related to the flow by

$$\underline{\boldsymbol{\tau}}_m = \mu_m\left[\nabla\mathbf{v}_m + (\nabla\mathbf{v}_m)^T - \frac{2}{3}\nabla\cdot\mathbf{v}_m\underline{\mathbf{I}}\right], \tag{5}$$

where μ_m is the viscosity of the silicates, assumed constant, and $\underline{\mathbf{I}}$, the identity tensor. The liquid metal is partly entrained by the matrix but also moves through the matrix according to a Darcy equation

$$c\Delta\mathbf{v} = \phi(\nabla P_f - \rho_f\mathbf{g}), \tag{6}$$

where c is related to the permeability $k(\phi)$ and the fluid viscosity μ_f by $c = \phi^2\mu_f/k(\phi)$. By using the Darcy relation, it seems that we necessarily imply that the metal percolates through a connected network. This is not necessarily so as the eq. (6) is general enough to even capture relative motion of isolated metal bubbles in the silicates (see, e.g. Batchelor 1967). The relative motion between the two phases can therefore be in agreement, through an appropriate choice of the parameter c, with the model of interacting droplets used by Höink *et al.* (2006).

The silicate and metal pressures P_m and P_f are different (and different from the average pressure of the silicate–metal mixture $\overline{P}$). A micromechanical model (see, e.g. Bercovici *et al.* 2001) suggests that they are related by

$$\phi\Delta P = -K\mu_m\nabla\cdot\mathbf{v}_m, \tag{7}$$

where K of order 1 is related to the topology of the melt–matrix interface and we take $K = 1$ in the following.

Assuming that the gravity is vertical and time-independent, the mechanical equations can be somewhat simplified by defining a total non-hydrostatic pressure Π,

$$\nabla\Pi = \nabla\overline{P} - \rho_m\mathbf{g} = \nabla[\phi P_f + (1-\phi)P_m] - \rho_m\mathbf{g}. \tag{8}$$

A similar reduction of pressure was used by Katz *et al.* (2007) (their ∇P^* corresponds to $\nabla P_m - \rho_m\,\mathbf{g}$ in our notation). Using this definition of Π, the total momentum equilibrium (4) becomes

$$-\nabla\Pi + \nabla\cdot[\mu^*\underline{\boldsymbol{\tau}}_m] - \phi\Delta\rho\mathbf{g} = 0, \tag{9}$$

showing that the matrix motion is controlled by the variation of silicate–metal proportion. The difference between the densities $\Delta\rho = \rho_m - \rho_f$ is negative and its magnitude is comparable to each separate density [i.e. $|\Delta\rho| \sim (\rho_m + \rho_f)/2$] which precludes using the usual Boussinesq approximation valid when the density variations are negligible compared to the average density.

Using the mass conservation eq. (1), the definition of Π, (8), and the expression of the pressure jump, (7), the Darcy eq. (6) can be recast as

$$\phi\Delta\mathbf{v} = \frac{\phi^2}{c}\left\{\nabla\left[\Pi + \frac{1-\phi}{\phi}\mu_m\nabla\cdot(\phi\Delta\mathbf{v})\right] + \Delta\rho\mathbf{g}\right\}. \tag{10}$$

The mechanical equations are supplemented by the energy balance. We assume $\rho_f C_f = \rho_m C_m = \overline{\rho}C$ for the heat capacities C_f and C_m, and the energy equation is

$$\overline{\rho}C\frac{\mathrm{D}T}{\mathrm{D}t} = Q + k_T\nabla^2 T + \mu_m\frac{1-\phi}{\phi}(\nabla\cdot\mathbf{v}_m)^2 + c(\Delta\mathbf{v})^2 + \mu^*\underline{\boldsymbol{\tau}}_m : \nabla\mathbf{v}_m, \tag{11}$$

where Q are the radioactive heat sources and k_T the average coefficient of thermal conductivity. The various sources of heat related to the flow dissipation are neglected in the usual Boussinesq approximation (Hewitt *et al.* 1975; Ricard 2007). However, in our case the separation of the two phases induces a change in potential energy dissipated as heat that must not be neglected.

2.2 Non-dimensionalization

We non-dimensionalize lengths by a length R (later identified with a planet radius), velocities by the two-phase Stokes velocity $|\Delta\rho|g_0R^2/\mu_m$, where g_0 is a reference gravity, time by $\tau = \mu_m/(|\Delta\rho|g_0R)$, pressures by $|\Delta\rho|g_0R$ and temperatures by $\theta = |\Delta\rho|g_0R/(\overline{\rho}C)$. This temperature scale is related to the gravitational energy that can be release by segregation (a better estimate of the change in gravitational energy during segregation is $(1/2)\phi(1-\phi)\theta$ which cancels as expected, for single phase planets, and is only $\sim$10 per cent of θ, but this would made the normalization unnecessarily complex).

Using this scaling, we get

$$-\nabla\Pi + \nabla\cdot[\mu^*\underline{\boldsymbol{\tau}}_m] + \phi\hat{\mathbf{g}} = 0, \tag{12}$$

$$\phi\Delta\mathbf{v} = \delta^2\phi^2\left\{\nabla\left[\Pi + \frac{1-\phi}{\phi}\nabla\cdot(\phi\Delta\mathbf{v})\right] - \hat{\mathbf{g}}\right\}, \tag{13}$$

$$\frac{\mathrm{D}T}{\mathrm{D}t} = \frac{\nabla^2 T}{Ra} + \frac{1-\phi}{\phi}(\nabla\cdot\mathbf{v}_m)^2 + \frac{(\Delta\mathbf{v})^2}{\delta^2} + \mu^*\underline{\boldsymbol{\tau}}_m : \nabla\mathbf{v}_m, \tag{14}$$

while the continuity and porosity evolution equations, (1) and (2), remain unchanged. In (12) and (13), $\hat{\mathbf{g}} = \mathbf{g}/g_0$ is the normalized gravity. The other dimensionless parameters are the Rayleigh number,

$$Ra = \frac{\overline{\rho}C\Delta\rho g_0R^3}{k_T\mu_m}, \tag{15}$$

the non-dimensionalized compaction length δ defined by

$$\delta^2 = \frac{\mu_m}{cR^2}, \tag{16}$$

and the viscosity of the mixture,

$$\mu^* = 1-\phi. \tag{17}$$

2.3 From two to three phases: melting of the metallic phase

The previous equations were presented assuming that the metallic phase was liquid (i.e. molten) and that the viscous shear stress was only supported by the silicate solid matrix. It is also possible to treat the case where the metal is either liquid or solid by using a temperature dependent interaction coefficient c such that $c^{-1} = 0$ below the iron melting temperature. Below the melting temperature, $\mathbf{\Delta v}$ (see eq. 10 when $c^{-1} = 0$), $\nabla\cdot\mathbf{v}_m$ (see eq. 1 when $\mathbf{\Delta v} = 0$) and $\nabla\cdot\mathbf{v}_f$ are identically equal to zero and the two phases are locked

Table 1. Typical parameter values for numerical models of two phase segregation.

Planet radius	R	2000	km
Silicate density	ρ_m	3200	$\mathrm{kg\,m^{-3}}$
Metal density	ρ_f	7000	$\mathrm{kg\,m^{-3}}$
Heat capacity	C	1000	$\mathrm{J\,K^{-1}\,kg^{-1}}$
Heat conductivity	k_T	3	$\mathrm{W\,m^{-1}\,K^{-1}}$
Initial temperature	T_0	1100	K
Iron melting temperature	T_{melt}	1300	K
Initial metal content	ϕ_0	0.25	
Silicate viscosity	μ_m	10^{19}	Pa s
Solid iron viscosity	μ_m	10^{19}	Pa s
Liquid iron viscosity	μ_f	1	Pa s
Permeability	$k_0(k = k_0\phi^2)$	4×10^{-9}	$\mathrm{m^2}$
Average density	$\overline{\rho} = \phi\rho_f + (1-\phi_m)\rho_m$	4150	$\mathrm{kg\,m^{-3}}$
Gravity	$g_0 = 4/3\pi G\bar{\rho}R$	2.32	$\mathrm{m\,s^{-2}}$
Temperature excess	ΔT	258	K
Temperature scale	$\theta = \Delta\rho g_0 R/(\overline{\rho}C)$	4247	K
Stokes velocity scale	$\Delta\rho g_0 R^2/\mu_m$	111	$\mathrm{km\,yr^{-1}}$
Timescale	$\mu_m/\Delta\rho g_0 R$	18	yr
Darcy separation velocity	$k_0\Delta\rho g_0\phi_0^2(1-\phi_0)/\mu_f$	58	$\mathrm{m\,yr^{-1}}$
Compaction length	$\sqrt{k_0\mu_m/\mu_f}$	210	km
Normalized comp. length	δ	0.1	
Rayleigh number	Ra	10^{10}	

together. In this case the parameter μ^* in front of $\underline{\boldsymbol{\tau}}_m$ should become the average normalized viscosity of the undifferentiated mixture instead of $1-\phi$, and eq. (12) becomes the usual Navier–Stokes equation for a single-phase continuum with compositional forcing. With $\boldsymbol{\Delta}\mathbf{v} = 0$ and $\boldsymbol{\nabla}\cdot\mathbf{v}_m = 0$, the energy equation becomes the usual single phase equation.

Assuming that the viscosities of the pure silicate matrix and of the undifferentiated iron–silicate mixture in solid state are equal, we can therefore account for the presence of molten iron by adding to the eqs (12)–(14) the following conditions:

(1) In regions below the iron melting temperature

(i) $c^{-1} = 0$, or in non-dimensional equations $\delta^2 = 0$
(ii) $\mu^* = 1$

(2) In regions above the iron melting temperature

(i) c finite, in non-dimensional equations $\delta^2 > 0$
(ii) $\mu^* = 1-\phi$

The melting or freezing of the metallic phase are treated in a very simplified way. At each point the metal phase is assumed to be either completely liquid or completely solid, depending on local temperature; there is no partially molten iron. In either case ϕ denotes the volume fraction of metal and it is identical to porosity when the metal is molten; in the following we loosely use the terms porosity and metallic volume fraction interchangeably. A unique, pressure-independent iron melting temperature $T_{\mathrm{melt}} = 1300\,\mathrm{K}$ is used (Table 1). The densities of the solid and liquid iron are assumed equal. This assumption is equivalent to maintaining the average velocity $\overline{\mathbf{v}}$ divergence free (eq. 1) irrespective of the physical state of the metallic phase. Including a density difference between solid and molten metal $\Delta\rho_f$ would result in an additional term in (1) proportional to $\Delta\rho_f\Gamma$ (Γ being the melting rate), and hence a non-solenoidal mixture velocity. This would greatly complicate the numerical resolution of the equations. We therefore adopt the assumption of no volume change upon phase change. This is reasonable as $\Delta\rho_f$ is at least an order of magnitude smaller than $\Delta\rho$.

The melting or freezing of the iron phase should consume or release latent heat. This energy term is neglected in the energy eq. (14) (see Šrámek *et al.* 2007, for details). Neglecting the latent heat is a crude approximation. The total sensible heat variation is $\overline{\rho}C\Delta T$, and the latent heat of the metal phase $\rho_f\phi L$. Using the parameters in Table 1 and taking $L = 240\,\mathrm{kJ\,kg^{-1}}$, the latent heat term represents an equivalent temperature difference of about 100 K. This value of latent heat of fusion L is for pure iron and should be significantly lower for iron alloys that melt at much lower temperature; the equivalent temperature difference may therefore be smaller. Certainly latent heat should be included in the future, and another variable, the volume fraction of molten iron, will have to be included and monitored.

2.4 Numerical resolution

The set of eqs (1), (2), (12)–(14) is solved in 2-D with Cartesian geometry. We decompose the matrix velocity $\mathbf{v}_m$ into incompressible and irrotational parts $\mathbf{v}_1$ and $\mathbf{v}_2$ and introduce two scalar functions Ψ_1 and Ψ_2 such that

$$\mathbf{v}_m = \mathbf{v}_1 + \mathbf{v}_2 = \left(-\frac{\partial\Psi_1}{\partial z} + \frac{\partial\Psi_2}{\partial x},\ \frac{\partial\Psi_1}{\partial x} + \frac{\partial\Psi_2}{\partial z}\right); \tag{18}$$

Ψ_1 is therefore the stream function of the incompressible flow and Ψ_2 the potential of the compressible irrotational flow. The convective flow $\mathbf{v}_1$ is tangent to the isolines of Ψ_1, the compaction flow $\mathbf{v}_2$ is perpendicular to the level lines of Ψ_2. The matrix velocity divergence is only related to Ψ_2 through a Poisson's equation

$$\boldsymbol{\nabla}\cdot\mathbf{v}_m = \boldsymbol{\nabla}\cdot(\phi\boldsymbol{\Delta}\mathbf{v}) = \boldsymbol{\nabla}\cdot\mathbf{v}_2 = \nabla^2\Psi_2. \tag{19}$$

Taking the curl of (12) and assuming uniform vertical gravity, one gets

$$\mu^*\nabla^4\Psi_1 + \mathcal{F}(\Psi_1) = -\frac{\partial\phi}{\partial x} + \mathcal{G}(\Psi_2), \tag{20}$$

where the two operators $\mathcal{F}$ and $\mathcal{G}$ are

$$\mathcal{F}(\Psi_1) = 2\boldsymbol{\nabla}\mu^*\cdot\boldsymbol{\nabla}\left[\nabla^2\Psi_1\right] + \widetilde{\nabla}^2\mu^*\widetilde{\nabla}^2\Psi_1 + 4\frac{\partial^2\mu^*}{\partial x\partial z}\frac{\partial^2\Psi_1}{\partial x\partial z}, \tag{21}$$

and

$$\mathcal{G}(\Psi_2) = 2\Bigg(\frac{\partial\mu^*}{\partial z}\frac{\partial}{\partial x}\nabla^2\Psi_2 - \frac{\partial\mu^*}{\partial x}\frac{\partial}{\partial z}\nabla^2\Psi_2 - \frac{\partial^2\mu^*}{\partial x\partial z}\widetilde{\nabla}^2\Psi_2 + \widetilde{\nabla}^2\mu^*\frac{\partial^2\Psi_2}{\partial x\partial z}\Bigg), \tag{22}$$

where

$$\widetilde{\nabla}^2 = \frac{\partial^2}{\partial z^2} - \frac{\partial^2}{\partial x^2}. \tag{23}$$

The operators $\mathcal{F}$ and $\mathcal{G}$ cancel out when the viscosity μ^* is uniform.

From Ψ_1 and Ψ_2, we compute the pressure gradient needed in the Darcy eq. (13) that we rewrite as

$$\begin{aligned}
&\left\{1 - \delta^2\phi^2\left[\frac{4}{3}\mu^*\frac{\partial^2}{\partial x^2} + \frac{\partial}{\partial x}\left(\frac{1-\phi}{\phi}\frac{\partial}{\partial x}\right)\right]\right\}\phi\Delta v_x = \delta^2\phi^2\mathcal{S}_x,\\
&\left\{1 - \delta^2\phi^2\left[\frac{4}{3}\mu^*\frac{\partial^2}{\partial z^2} + \frac{\partial}{\partial z}\left(\frac{1-\phi}{\phi}\frac{\partial}{\partial z}\right)\right]\right\}\phi\Delta v_z\\
&\quad = -\delta^2\phi^2(1-\phi) + \delta^2\phi^2\mathcal{S}_z,
\end{aligned} \tag{24}$$

where the two source terms are

$$\begin{aligned}
\mathcal{S}_x &= -\mu^*\frac{\partial\nabla^2\Psi_1}{\partial z} + \frac{4}{3}\mu^*\frac{\partial^2}{\partial x\partial z}\phi\Delta v_z + \frac{\partial}{\partial x}\left(\frac{1-\phi}{\phi}\frac{\partial}{\partial z}\phi\Delta v_z\right)\\
&\quad - 2\frac{\partial\mu^*}{\partial x}\left(\frac{\partial^2\Psi_1}{\partial x\partial z} - \frac{2}{3}\frac{\partial^2\Psi_2}{\partial x^2} + \frac{1}{3}\frac{\partial^2\Psi_2}{\partial z^2}\right)\\
&\quad + \frac{\partial\mu^*}{\partial z}\left(\frac{\partial^2\Psi_1}{\partial x^2} - \frac{\partial^2\Psi_1}{\partial z^2} + 2\frac{\partial^2\Psi_2}{\partial x\partial z}\right),\\
\mathcal{S}_z &= +\mu^*\frac{\partial\nabla^2\Psi_1}{\partial x} + \frac{4}{3}\mu^*\frac{\partial^2}{\partial x\partial z}\phi\Delta v_x + \frac{\partial}{\partial z}\left(\frac{1-\phi}{\phi}\frac{\partial}{\partial x}\phi\Delta v_x\right)\\
&\quad + \frac{\partial\mu^*}{\partial x}\left(\frac{\partial^2\Psi_1}{\partial x^2} - \frac{\partial^2\Psi_1}{\partial z^2} + 2\frac{\partial^2\Psi_2}{\partial x\partial z}\right)\\
&\quad + 2\frac{\partial\mu^*}{\partial z}\left(\frac{\partial^2\Psi_1}{\partial x\partial z} - \frac{1}{3}\frac{\partial^2\Psi_2}{\partial x^2} + \frac{2}{3}\frac{\partial^2\Psi_2}{\partial z^2}\right).
\end{aligned} \tag{25}$$

In (24), the driving forces of the right-hand side are related to the density difference between the two phases (Hernlund & Tackley 2007) but also to the pressure gradients (implicitly in $\mathcal{S}_x$ and $\mathcal{S}_z$) that are essential to focus the liquid phase towards the regions of matrix divergence (Spiegelman & McKenzie 1987).

In our finite difference numerical code the variables are discretized on a staggered grid where Ψ_1 is at the corners, and Ψ_2, ϕ and T at the centre of the grid cells. The vertical velocities v_{mz}, v_{fz} and $\phi\Delta v_z$ are evaluated in the middle of the horizontal sides, the horizontal velocities v_{mx}, v_{fx} and $\phi\Delta v_x$ in the middle of the vertical sides. This grid insures that all the spatial derivatives are second order accurate (Patankar 1980). We start the computation with a first guess of Ψ_2. We solve for Ψ_1 using (20) by putting all the finite difference expressions of the operator $\nabla^4 + \mathcal{F}$ into a single large matrix that is exactly inverted. The Darcy eq. (13) is then solved iteratively using an alternating direction implicit method on the coupled eqs (24) (iterations for the Darcy equation); as a convergence criterion, we require that the rms value of the Darcy velocity ($\phi\mathbf{\Delta v}$) difference between two iteration steps falls below a prescribed limit (equal to 10^{-9} in our calculations). The divergence of the total matrix velocity is then computed and a new estimate of Ψ_2 is obtained by solving Poisson's eq. (19). This process is repeated until the convergence of the mechanical equations (iterations for the Navier–Stokes equation). Porosity and temperature are then updated from (2) and (14) using a scheme specifically discussed in Appendix A as the absence of diffusion in the porosity equation makes the discretization of this equation potentially unstable.

The choice of boundary conditions is somewhat problematic. Ideally one would like to ascribe conditions directly on the average velocity and total stresses. This would couple the boundary conditions of (19), (20) and (24). For simplicity we implement separately the boundary conditions for the incompressible and irrotational components of $\mathbf{v}_m$. We use impermeable free slip conditions for both $\mathbf{v}_1$ and $\mathbf{v}_2$, therefore for $\mathbf{v}_m$. In addition, the boundary is also impermeable for the fluid phase.

The time of execution of the program can be decreased by orders of magnitude if one assumes $\mu^* = 1$ (uniform viscosity approximation). In this case the term $\mathcal{G}(\Psi_2)$ is zero. This decouples the eq. (20) for Ψ_1 and avoids the Navier–Stokes iterations. Moreover, the term $\mathcal{F}(\Psi_1)$ in the same equation is also zero which allows to compute and store the matrix corresponding to the inverse of Navier–Stokes operator ∇^4 just once. A more accurate approximation is to keep a non-zero $\mathcal{F}(\Psi_1)$ (i.e. to account for lateral viscosity variations in the incompressible flow) but neglect $\mathcal{G}(\Psi_1)$ (i.e. the coupling between the incompressible and compressible flows). This approximation also avoids the Navier–Stokes iterations but the operator, $\nabla^4 + \mathcal{F}$, has to be computed at each time step. This approximation is very similar to that done by Schmeling (2000) and we use his terminology of 'compaction Boussinesq approximation'. The approximations are summarized as follows:

Full solution

(i) Both $\mathcal{F}(\Psi_1)$ and $\mathcal{G}(\Psi_2)$ are kept.
(ii) $\mu^* = 1 - \phi$
(iii) The solutions of Ψ_1 and Ψ_2 are coupled, and the matrix of the operator $\nabla^4 + \mathcal{F}$ has to be calculated several times in each time step until the combined solution for Ψ_1 and Ψ_2 converges.

Compaction Boussinesq approximation

(i) $\mathcal{G}(\Psi_2)$ is put equal to zero, but $\mathcal{F}(\Psi_1)$ is kept.
(ii) This corresponds to writing $\mu^*\underline{\boldsymbol{\tau}}_m = \mu_1^*\underline{\boldsymbol{\tau}}_1 + \mu_2^*\underline{\boldsymbol{\tau}}_2$, where $\underline{\boldsymbol{\tau}}_1 = \underline{\boldsymbol{\tau}}_1(\mathbf{v}_1)$ and $\underline{\boldsymbol{\tau}}_2 = \underline{\boldsymbol{\tau}}_2(\mathbf{v}_2)$, in the momentum eq. (12) and the energy eq. (14), with $\mu_1^* = 1 - \phi$ and $\mu_2^* = 1$. In other words, the lateral viscosity variations are accounted for in the incompressible flow, but the compressible flow is computed with a uniform viscosity.
(iii) The solutions of Ψ_1 and Ψ_2 are decoupled, but the matrix of the operator $\nabla^4 + \mathcal{F}$ has to be calculated once for each time step because $\mathcal{F}$, which depends on $\partial\mu_1^*$, evolves.

Uniform viscosity approximation

(i) Both $\mathcal{F}(\Psi_1)$ and $\mathcal{G}(\Psi_2)$ are put equal to zero.
(ii) This corresponds to having $\mu^* = 1$.
(iii) The solutions of Ψ_1 and Ψ_2 are decoupled, and the matrix of the operator $\nabla^4 + \mathcal{F}$ is only calculated once.

2.5 Benchmark of the code

Most crudely viewed, the numerical resolution consists of repeating two principal steps. The first step is solving the momentum equations for the velocity fields with a given porosity and temperature. The discretization of the dynamical equations is second order in space. Accordingly, we verified that the accuracy of the solution increases linearly with the square of the mesh size. The second step is the advancement of porosity and temperature in time, which we discuss in Appendix A.

We also check the global energy budget of our simulations. With the impermeable, free-slip condition on the boundary of the

calculation domain ($\mathbf{v}_f \cdot \hat{\mathbf{n}} = 0$, $\mathbf{v}_m \cdot \hat{\mathbf{n}} = 0$, $\mathbf{v}_m \cdot \underline{\boldsymbol{\tau}}_m \cdot \hat{\mathbf{n}} = 0$, where $\hat{\mathbf{n}}$ is a vector normal to the boundary) the energy can be transferred across the boundary only by heat conduction.

Let us consider a reference (e.g. initial) porosity and temperature distribution which give reference values for the total potential and thermal energies. The change in total potential energy in the calculation domain is

$$\delta\widetilde{E}_p = -\int_{\widetilde{V}} |\Delta\rho|\delta\phi g_0 \widetilde{z}\, \mathrm{d}\widetilde{V}, \quad \text{or} \quad \delta E_p = -\int_V z\delta\phi\, \mathrm{d}V; \tag{26}$$

likewise the change in thermal energy is

$$\delta\widetilde{E}_T = \int_{\widetilde{V}} \overline{\rho} C \delta\widetilde{T}\, \mathrm{d}\widetilde{V}, \quad \text{or} \quad \delta E_T = \int_V \delta T\, \mathrm{d}V, \tag{27}$$

where $\delta\phi$ and δT are porosity and temperature deviations from the reference profiles. Quantities with a tilde are dimensional, without a tilde non-dimensionalized, δE_p and δE_T are non-dimensionalized with $|\Delta\rho|g_0 R^4$ (for a 3-D domain). The integration is carried over the entire volume.

The conservation of the total energy is then expressed as

$$\frac{\mathrm{d}}{\mathrm{d}t}\int_V (T - z\phi)\mathrm{d}V = Ra\, Q, \tag{28}$$

where

$$Q = \oint_{\delta V} \hat{\mathbf{n}} \cdot \boldsymbol{\nabla} T\, \mathrm{d}A \tag{29}$$

is the non-dimensional integrated heat flux across the outer boundary δV of the calculation domain. For a thermally isolated domain (i.e. with a boundary condition on temperature $\hat{\mathbf{n}} \cdot \boldsymbol{\nabla} T = 0$) the total energy in the domain remains constant. For all our simulations the global energy budget (28) is very accurately satisfied within a few per cent (see Section 4.5).

3 CORE FORMATION TRIGGERED BY IMPACT MELTING

We study the situation where a growing planet embryo made of metal and silicates in the solid state, is struck by an impact that locally brings the temperature above the metal melting temperature. It is well known that the segregation of metal liberates a gravitational energy per unit mass comparable to that brought by an impact. As suggested by Ricard *et al.* (2009), this is potentially able to generate a runaway instability resulting in large-scale differentiation.

When an impactor of mass m_i hits a planet, it buries a fraction f_1 of its kinetic energy into a domain of mass $m = f_2 m_i$. The rest of the kinetic energy is rapidly radiated away and may heat up the primitive atmosphere (Matsui & Abe 1986a). The two factors f_1 and f_2 are not well known but have been estimated from experiments and models to be $f_1 \sim 1/3$ and $f_2 \sim 6$, that is, one third of the kinetic energy heats up rather homogeneously a volume six times larger than that of the impactor (Pierazzo *et al.* 1997; O'Keefe & Ahrens 1999; Monteux *et al.* 2007). The volume heated by the shock wave that follows the impact, often called the isobaric core, is roughly spherical and tangent to the surface at the impact point (Melosh 1996). The escape velocity of a growing planet of radius R and surface gravity g, $\sqrt{2gR}$, should be indicative of the average impact velocity (e.g. Tonks & Melosh 1992). As $g = 4/3\pi G\overline{\rho}R$, where G is the gravitation constant and $\overline{\rho}$ the average density, the energy deposited as heat in the target planet, per unit mass of the impact core, is therefore (Ricard *et al.* 2009)

$$\Delta E_1 = \frac{4\pi f_1}{3 f_2}\overline{\rho} G R^2. \tag{30}$$

This amounts to $\Delta E_1[\mathrm{J\,kg^{-1}}] \sim 6.4 \times 10^{-2} \times (R[\mathrm{km}])^2$ for a planet of average density $\overline{\rho} = 4150\,\mathrm{kg\,m^{-3}}$ (see Table 1). For example, assuming the iron does not melt, this corresponds to a temperature increase of 260 K for a planet of 2000 km, where we took the heat capacity $C = 1000\,\mathrm{J\,K^{-1}\,kg^{-3}}$. Alternatively, as soon as the planet reaches 1300 km, this energy is enough to provide the latent heat necessary to melt all the iron content of the impacted zone (25 per cent volume iron with latent heat $L = 240\,\mathrm{kJ\,kg^{-1}}$). The melting temperature of pure iron is around 1800 K at atmospheric pressure. This temperature is reduced in the presence of impurities to 1200–1300 K and increases under pressure (Fei *et al.* 1997; Agee *et al.* 1995). At this temperature, the mantle peridotite is still below its solidus (Hirschmann 2000).

The amount of thermal energy delivered by an impact can be compared to the energy dissipated by forming the core. The gravitational energy E_g of a planet of density $\rho(r)$ and radius R is (Solomon 1979)

$$E_g = -16\pi^2 G \int_0^R \int_0^r \rho(r)\rho(u) r u^2\, \mathrm{d}u\, \mathrm{d}r. \tag{31}$$

This corresponds to the energy needed for successively bringing from infinity the infinitesimal shells constituting the planet. The segregation of an undifferentiated planet, by changing the density profile, decreases the gravitational energy. The difference of gravitational energy between the undifferentiated and the differentiated situations being related to processes occurring inside the planet, is released in the form of thermal energy (Flasar & Birch 1973; Davies 1980).

From (31), the segregation of an undifferentiated planet of density $\overline{\rho} = \phi\rho_f + (1-\phi)\rho_m$ into a core of density ρ_f and a mantle of density ρ_m releases, per unit mass of the planet, the energy (Ricard *et al.* 2009)

$$\Delta E_2 = \frac{4G\pi R^2}{5\overline{\rho}}\Big[\overline{\rho}^2 - \rho_f^2\phi^{5/3} - \rho_m^2(1-\phi^{5/3}) - \frac{5}{2}(\rho_f - \rho_m)\rho_m\phi(1-\phi^{2/3})\Big]. \tag{32}$$

This energy release cancels out when $\phi = 0$ (no metal), $\phi = 1$ (no silicates) or $\rho_m = \rho_f$ (no differentiation) which are three cases where segregation is not meaningful. Typically for a planet containing 25 per cent of metal in volume ($\phi = 0.25$), $\rho_f = 7000\,\mathrm{kg\,m^{-3}}$ and $\rho_m = 3200\,\mathrm{kg\,m^{-3}}$, $\Delta E_2[\mathrm{J\,kg^{-1}}] \sim 5.8 \times 10^{-2} \times (R[\mathrm{km}])^2$. Therefore the specific thermal energy deposition during an impact on a planet is comparable to the thermal energy release associated with the metal segregation.

This simple numerical application shows that as both ΔE_1 and ΔE_2 increase with R^2, it is impossible for a growing planet to reach a large size without undergoing the melting of its metallic content in its shallow layers. It also shows that when segregation starts, the heating associated with the energy dissipation is sufficient to melt the metal content in a comparable amount of undifferentiated material, which lead to the runaway instability described in Ricard *et al.* (2009).

4 POST IMPACT EVOLUTION

4.1 Parameter values

To simulate the post-impact evolution we consider a rather small proto-planet (radius $R = 2000$ km) with a uniform temperature of 1100 K. This gives a surface gravity $g_0 = 2.3\,\mathrm{m\,s^{-2}}$, and a temperature scale of $\theta = |\Delta\rho|g_0 h/(\overline{\rho}C) = 4247$ K. The energy buried in

the isobaric core after the impact is $\Delta E = 260\,\mathrm{kJ\,kg^{-1}}$ (see eq. 30). This corresponds to a temperature increase of $\Delta T = 260\,\mathrm{K}$ assuming all this energy is used to heat up the impact zone. If we accounted properly for the energy consumed upon melting, some 40 per cent of ΔE would be required to melt all the metal in the isobaric core, the rest being available for a temperature increase of 150 K. In our code which neglects the latent heat of fusion the initial temperature of the planet T_0 (assumed uniform) must be at least $T_{\mathrm{melt}} - \Delta T = 1040\,\mathrm{K}$, so that the metallic phase melts after the impact and can separate from the silicates. In the following simulations we use an initial planet temperature of 1100 K. All parameter values are summarized in Table 1.

For simplicity, the initial state is undifferentiated with an initial volumetric metal content of 25 per cent, which is somewhat larger than Earth's content (∼18 per cent) but much smaller than Mercury's content. It is also possible that the impacting meteorites have already undergone some partial differentiation due to heating by short-lived radionuclides (Yoshino *et al.* 2003). Our assumption is that after the impact the fragmentation leads to rather even distribution of metal content, at least with respect to the numerical grid-size we use. We show some simulations with random initial metal distribution in Section 4.8.

We assume that the silicates remain solid but with a rather low viscosity of 10^{19} Pa s. This is clearly a parameter on which very little is known. We choose a rather small value because the silicates are already rather hot and because the deviatoric stresses due to the huge compositional density variation in the evolving planet should bring the rheology to non-linear regimes and reduce the equivalent viscosity by a large amount (Samuel & Tackley 2008). The viscosity of the metal–silicate mixture should also be reduced by the fact that the metal component is close to its melting temperature. When liquid metal is present, the mixture viscosity is further reduced by the factor $\mu^* = 1 - \phi$. A stronger porosity dependence of the viscosity could be used (e.g. Golabek *et al.* 2008) but we choose to keep the model as simple as possible. At very high molten metal fractions the solid grains may become disconnected (i.e. a suspension of solid particles in liquid metal). This transition in rheology is accompanied by a drastic decrease in viscosity (by many orders of magnitude given the difference between viscosities of solid silicates and molten metal). Accounting for this rheological transition presents further numerical difficulties for a code that already involves seven non-linear coupled differential equations. In any case, the rate of segregation will be controlled by the much slower separation in the regime of low-to-moderate liquid metal content where the solid remains interconnected. We assume that both phases are viscous fluids, albeit of very different viscosities; we have not considered more complex rheologies, such as viscoelasticity or fracture.

The chosen viscosity corresponds to a Rayleigh number of 10^{10}, although in most calculations we use $Ra = 10^6$. The timescale based on the Stokes velocity is very short (18 yr; the normalization uses the planetary radius to compute the Stokes velocity). The non-dimensionalized compaction length $\sqrt{\mu_m/(cR^2)}$ is a rather small number. The parameter c is $\mu_f\phi^2/k$ where k is a permeability (Bercovici *et al.* 2001). We use a permeability–porosity relationship in the form $k = k_0\phi^2$ (Bear 1988), where the permeability coefficient k_0 scales with the square of characteristic spacing of molten metal channels. Taking the silicate viscosity $\mu_f = 1$ Pa s and the permeability coefficient $k_0 = 4 \times 10^{-9}\,\mathrm{m^2}$ (channel spacing of ∼1 mm), we get a compaction length $\delta = 0.1$. The compaction length is the most uncertain parameter, given the uncertainties in μ_m, μ_f and k_0. Rather than explore the entire parameter space, in this study we chose a plausible set of parameters and discuss in detail the evolution of the new multi-phase segregation model for this specific case. We also investigate the effect of the impactor size, the target planet's size and its background temperature on the post-impact segregation.

4.2 Segregation of a proto-core

We first present a calculation of core segregation in a domain of aspect ratio 1 from an initial state where the metal–silicate component ratio is uniform. At $t = 0$ we increase the temperature in a circular zone close to the surface so that the temperature becomes higher than the melting temperature of iron. This initial condition crudely approximates the situation during the period where the surface of a planet embryo was heated by a giant impact (Wetherill 1985).

The radius of the initially heated zone is arbitrary 1/6 of the planetary radius (i.e. 333 km), which would be caused by an impactor of radius smaller by factor $f_2^{1/3} = 6^{1/3}$ (183 km). The complete separation of the metal from the silicates would generate an amount of pure metal corresponding to a sphere of radius $\phi_0^{-1/3}$ times smaller than the heated zone ($r = 210\,\mathrm{km}$). Two typical velocities involved in the segregation process are the Stokes velocity $v_S = 2|\Delta\rho|g_0r^2/(9\mu_m)$ of the metallic sphere and the Darcy separation velocity $v_D = |\Delta\rho|g_0\phi_0^2(1-\phi_0)/c$ of the two-phase porous flow. They amount to 82 and 58 m yr^{-1}, respectively. These velocities are small enough so that the approximation of an infinite Prandtl number (no inertia) is justified. It is however ∼1000 times faster that typical plate tectonics processes which suggests that the timescale of metal sinking is of the order of 10 kyr.

We assume a no heat flux boundary condition on top of our model. Another boundary condition would be very easy to implement but this insulation may be appropriate for a planet heated from the surface and where the atmosphere is very hot (Matsui & Abe 1986b). We also use the compaction Boussinesq approximation in most of our simulations. Surprisingly, the full solution and the two approximations discussed in Section 2.4 are quite similar as illustrated in Section 4.7. Neglecting the viscosity variations in the compaction flow only (compaction Boussinesq approximation) seems to be a good compromise that remains very close to the full solution but decreases the computation time by one order of magnitude by avoiding the coupling between the incompressible and irrotational components of the flow.

We have presented some results from this simulation, including some snapshots from Figs 1 and 2, in our previous work (Ricard *et al.* 2009). Here we present a full account and further analysis of the results. This simulation will be a reference case to which the simulations made with alternative choices of parameters will be compared to. Figs 1 and 2 show the evolution of metal content and temperature following an impact. Several stages of different prevailing segregation mechanisms can be identified in the simulation run. Initially the circular zone, containing the molten metallic phase, segregates by a roughly 1-D porous flow (Richter & McKenzie 1984). This 1-D compaction lasts for non-dimensional times $t = 0$–100 (0–1.8 kyr). The molten metal concentration increases to a value close to 1. The dense metallic blob is formed and eventually descends in a diapir-like fall ($t \sim 100$–500 or 1.8–9.0 kyr). The light residual silicate mantle rises and starts spreading as a gravity current along the surface. Similar spreading is exhibited by the metal when it reaches the bottom of the computation domain, thus forming a proto-core. A cusp-like channel connects the differentiated silicates to the core. A similar behaviour leading to the formation of trailing conduits has been documented

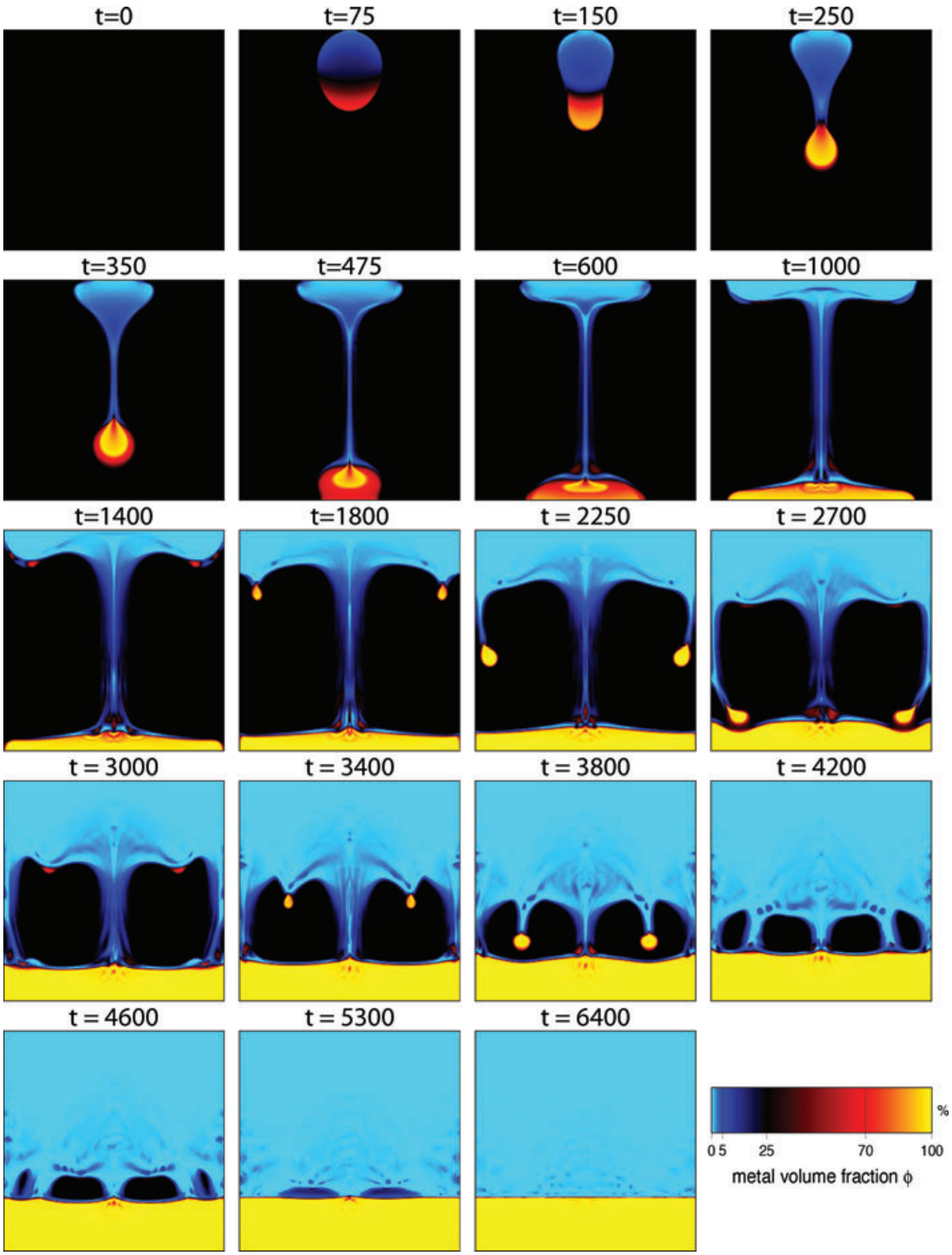

Figure 1. Evolution of the metal volume fraction after an impact in a square box calculation with a uniform initial composition. A circular zone of radius 1/6 is initially heated above the melting temperature of iron. We choose the colour scale so that the pure metallic phase is yellow, the pure silicate phase is cyan and the undifferentiated mantle is black. The normalized times are indicated. The dimensional values are obtained by multiplying with 18 yr. The compaction Boussinesq approximation is used on a regular grid with 300 × 300 grid cells.

experimentally (Olson & Weeraratne 2008). The gravitational energy released by the formation of the differentiated structure is converted into heat and increases the temperature. New pockets of metal are formed along the conduit and descend to the proto-core ($t \sim 1000$). The local temperature rise can induce further melting of the metallic phase and thus facilitates further segregation. At the interface between the differentiated silicate and the remaining undifferentiated mantle new metallic ponds are formed ($t \sim 1100$–1300) that trigger new instabilities ($t \sim 1400$–1500). These secondary instabilities follow the same kind of dynamics as the initial one with

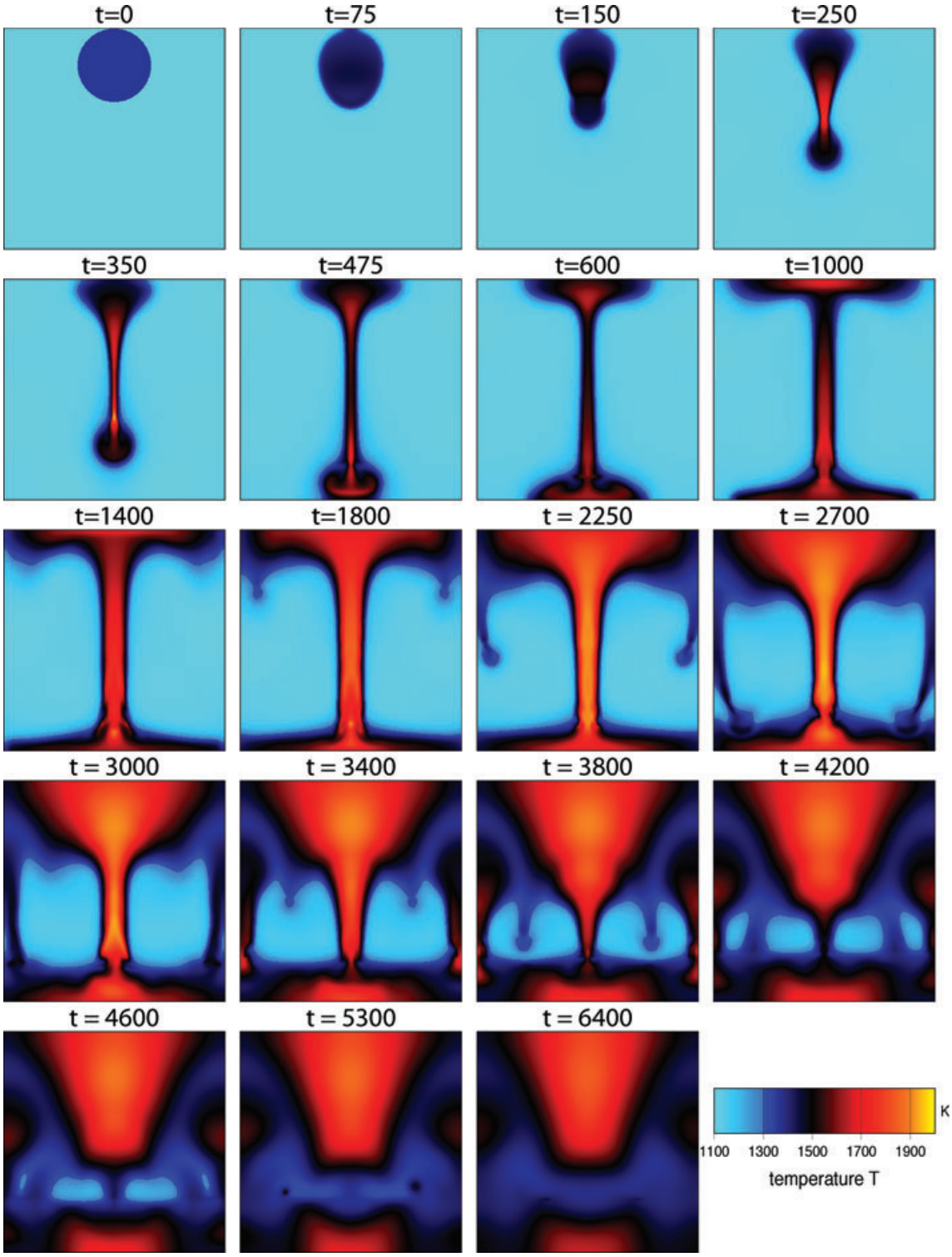

Figure 2. Evolution of temperature. Parameters of the calculation are given in the caption of Fig. 1.

cusp-like trailing conduits ($t \sim 2000$–3000) connecting them to the surface. The same process, that is, the creation of metallic ponds and descent of diapirs, occurs again ($t \sim 3000$–4500). Large undifferentiated islands survive for some time ($t \sim 4500$–5500) and are slowly eroded until the whole planet is differentiated ($t \sim 6000$ or 108 kyr). During the whole process various compaction waves are visible in both the silicates and the core (e.g. Scott & Stevenson 1984; Hier-Majumder *et al.* 2006).

The process just described can be followed both on the metal content, Fig. 1, and on the temperature, Fig. 2. The transfer of potential energy into thermal energy will be discussed in detail in Section 4.5; we particularly show in Fig. 5 that the global energy conservation is very closely satisfied throughout the whole simulation. This conversion occurs mostly along the channels trailing behind the diapirs. The heat seems to be transferred more or less equally between the core and the shallow mantle. After $t \sim 3000$

when only the deep mantle remains undifferentiated the rate of release of potential energy gradually decreases in amplitude, and after $t \sim 4000$ the erosion of the last cold undifferentiated regions occurs by thermal diffusion.

4.3 Vertical profiles and energy partitioning

Fig. 3 shows the metal fraction ϕ (top panel) and temperature T (bottom panel) as functions of depth at several times during the core segregation. The solid curves correspond to laterally averaged profiles, and the only dashed line in the top panel corresponds to a vertical profile in the middle of the computation domain. The black dashed curve in the top panel shows metal fraction during the first diapir's descent with the propagating front of the diapir, which is basically of pure metal. The conduit left behind the diapir is depleted in metal and a smaller compositional waveforms that will further decrease the metal content in the trailing conduit. The horizontally averaged metal fraction gradually evolves into a step-like function near the completion of segregation (blue curve). The inset in the top panel shows the average metal fraction in the core volume (bottom 25 per cent of the calculation domain) as a function of time. The three kinks in the curve marked by orange arrows at times 320, 2440 and 3800 correspond to the arrival of the large

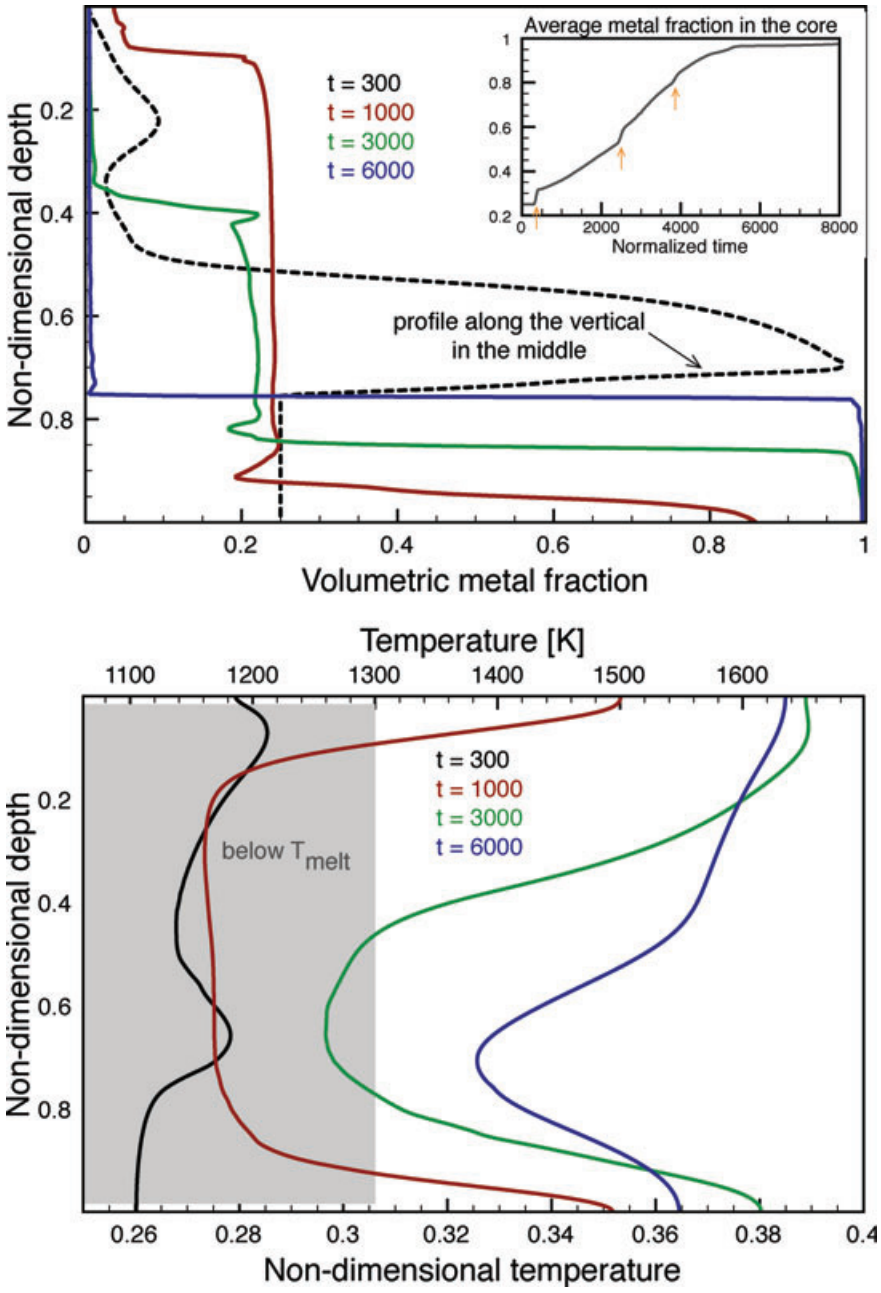

Figure 3. Volumetric metal fraction ϕ (top panel) and temperature T (bottom panel) as functions of depth. Horizontally averaged metal fraction and temperature are shown as solid lines. The dashed line in the top panel shows the metal fraction along the vertical in the centre of the calculation domain. Color marks different instants in time (normalized time 300 in black, 1000 in red, 3000 in green, 6000 in blue). The inset in the top panel shows the average metal fraction in the core volume (bottom 25 per cent of the calculation domain) with respect to time.

diapirs (primary, secondary and tertiary instabilities). The depth dependence of temperature in the bottom panel of Fig. 3 shows that the region at intermediate depths (corresponding to deep mantle) experiences on average less heating than the shallow mantle or the core. The final temperature, corresponding to the diffusion of the initial temperature anomaly and the release of gravitational energy is slightly above 1500 K, or 400 K above the initial temperature.

The maximum temperature reached in the simulation occurs in the trailing conduit for $t = 2420$. It amounts to 0.481 (2040 K). The maximum temperatures remain above 0.45 (1900 K) during time interval $t \sim 2010$–3420. With the low pressures involved in this small planet this should be enough to also melt a minor proportion of silicates. Although the latent heat of metal and silicate melting would moderate the temperature, the solidus of silicates should be reached in the shallowest 10–20 per cent of the planet (Hirschmann 2000). As we have totally neglected the thermal expansion no thermal convective instabilities can be present. This is probably reasonable for the silicates and the undifferentiated part of the planet as the thermal density anomalies are always very small (compared to compositional density anomalies) and as the duration of the segregation is very short. Thermal convection should occur in the core and would homogenize the core temperature. We have however not tried to account for these further complexities.

The partitioning of the released gravitational energy between the conduit itself and the adjacent regions and, consequently, between the mantle and the core has implications for the subsequent thermal evolution of the planet. The outcome of the numerical simulation can be compared to a result of a simple analysis. A blob of pure metal of volume V that descends from near surface to the bottom (a fall along distance R in a uniform gravity field) releases gravitational energy $\Delta\rho V g R$. Assuming all this energy remains in the iron blob and heats it up, we obtain an upper bound on temperature increase within the descending diapir. As temperature increase consumes the energy $\rho_f V C \Delta T$, we get

$$\Delta T_{\max}^{\text{diapir}} = \frac{\Delta\rho g R}{\rho_f C}, \tag{33}$$

or 2520 K (see Table 1 for numerical values). A characteristic lower bound on temperature increase (or average temperature increase) corresponds to a redistribution of the released gravitational energy uniformly across the planet. The Cartesian version of eq. (32) relevant to the simulation leads to

$$\Delta T_{\text{ave}} = \frac{\Delta\rho g R}{2\overline{\rho} C}\phi(1-\phi), \tag{34}$$

which amounts to 398 K.

As noted above, the maximum temperature reached in the simulation is 2040 K for an initial temperature of 1360 K in the impact zone and of 1100 K elsewhere. The maximum local temperature increase during the simulation $\Delta T_{\max}^{\text{simul}}$ is therefore between 680 and 940 K. This is about twice the average temperature increase. Comparison of $\Delta T_{\max}^{\text{simul}}$ and $\Delta T_{\max}^{\text{diapir}}$ suggests that 27–37 per cent of the potential energy release is dissipated within the metallic diapirs, while the remaining 73–63 per cent heats up the whole planet. The thermal energy brought to the core by the sinking diapirs should be quickly redistributed within the core by vigorous thermal convection.

We can compare this analysis to the simulation result. For example, at $t = 6400$ (when the differentiation is complete) the integration of the temperature indicates a similar average temperature in the mantle and in the core. This would suggest a simple core–mantle energy partitioning according to their respective volumes.

4.4 A new mechanism of metal diapir propagation

In the present simulation, the initial sinking of metallic blobs resembles the usual diapir instability in a simple single-phase medium. The physics, however, is rather different because a Darcy two-phase flow is superimposed on the Stokes flow. In order to elucidate the primary mechanisms of metal diapir propagation, we show in Fig. 4 the instantaneous full ($\mu^* = 1 - \phi$) solutions to the mechanical equations for four different cases of simple metal content and temperature distributions (i.e. we solve the Navier–Stokes equation, 12, and the Darcy equation, 13). In the first two rows, we show the prescribed temperature and metal content. Temperature is blue below iron melting temperature and red above. Metal content is 25 per cent (black) or 75 per cent (red). The third row shows the compaction rate [$\boldsymbol{\nabla}\cdot\mathbf{v}_m = \boldsymbol{\nabla}\cdot(\phi\boldsymbol{\Delta}\mathbf{v})$]. In the last row is the vertical velocity of the silicate matrix.

In case I (first column in Fig. 4), the situation corresponds to a simple single phase compositional diapir. The temperature is uniform and below the melting temperature of the iron phase. The metal content, and hence the density, is larger in the central circle. As the iron is solid, no segregation occurs. The compaction rate is zero. The velocity field is purely incompressible, only $\mathbf{v}_1$ is excited ($\mathbf{v}_m = \mathbf{v}_1$, $\mathbf{v}_2 = \mathbf{0}$; see eq. 18). The vertical component of silicate velocity (red when in the direction of gravity) shows the sinking of the dense diapir and the upwelling return flow of the lighter mixture. Although the matrix is lighter than the metal, in the diapir circle it is entrained downwards by the enhanced metallic content.

In case II (second column in Fig. 4), the porosity is increased in the circular region, but the temperature is now uniformly above the melting temperature of metal. The metallic phase can now separate from the silicates by compaction (middle row). This separation is the most efficient in the high porosity region but occurs also outside of this region. In particular, the deepest layers become enriched in metal, the shallowest ones depleted. The light silicates are globally rising (blue vertical velocity) but within and near the high metallic content region the downward average velocity of the mixture due to metal enrichment exceeds the separation velocity $\boldsymbol{\Delta}\mathbf{v}$. As a result the silicates are dragged downwards by the sinking metal in the metal enriched blob or at least their upward motion is impeded in the adjacent region. The general behaviour of this diapir is that of a solitary compaction wave (Spiegelman 1993; Wiggins & Spiegelman 1995; Rabinowicz *et al.* 2001).

In case III (third column in Fig. 4) the metal content is uniform but the temperature is above the iron melting temperature in the central region. Now the phase separation only occurs in the diapir, as outside the two phases are locked together. Within the diapir the silicates rise slowly. The matrix velocity is now purely irrotational (only $\mathbf{v}_2$ is excited, see eq. 18).

The last case IV (last column in Fig. 4) differs from case III by a large metallic content only in the central region. Like in case III, the two phases separate only in the circle, where the metal is liquid. However the presence of a density anomaly results in a velocity similar to case I (compositional single phase diapir). The matrix sinking velocity is decreased within the diapir as the silicates move upwards with respect to the average velocity. The sinking velocity of the undifferentiated matrix is enhanced in the front and in the wake of the diapir, which is in accord with the abrupt change in the compaction rate.

The case I corresponds to the simple sinking of a high density heterogeneity without phase segregation. If evolved in time, this metallic blob would sink and spread along the bottom, but it's metal content would remain unchanged. In order to separate the iron from

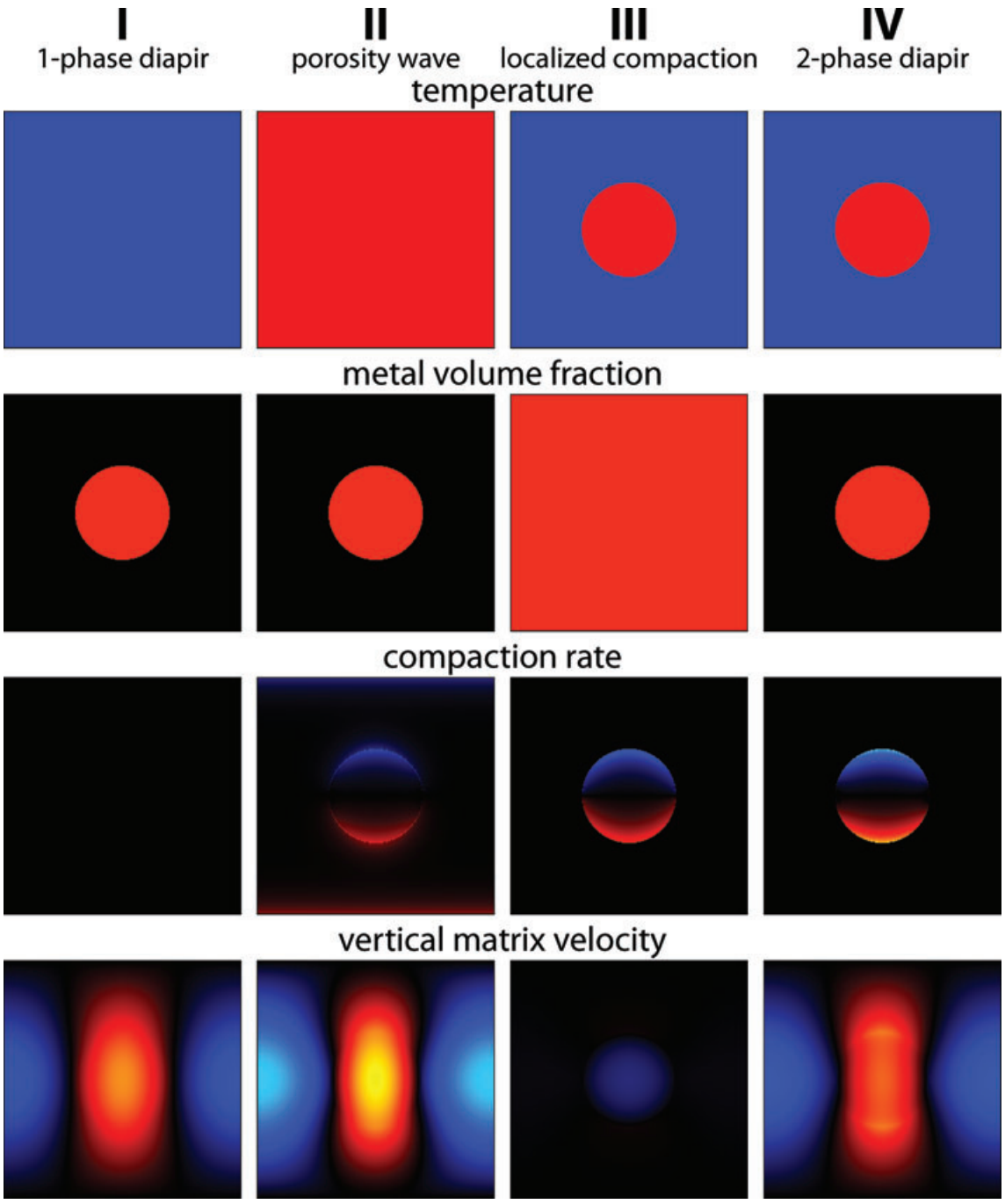

Figure 4. Temperature (first row), metal content (second row), compaction rate $\nabla \cdot \mathbf{v}_m = \nabla \cdot (\phi \Delta \mathbf{v})$ (third row) and vertical matrix velocity v_{m_z} (last row). The temperature is either below the iron melting temperature (blue) or above (red). The metal fraction is 25 per cent (black) or 75 per cent (orange). Two phase compaction only occurs where the metal is liquid. The same linear colour scale is used for the four panels (blue when compacting, red when dilating). The velocity field velocity field is purely incompressible in case I, purely irrotational in case III, and a superposition of both in cases II and IV. The same linear colour scale is used for the four panels (blue for upwellings, red for downwellings). The full solution with $\mu^* = 1 - \phi$ is calculated.

the silicates the temperature has to reach the melting temperature of iron (cases II–III–IV). This can happen locally in a small region (basically only within the diapir itself, cases III and IV). If the potential energy release of the sinking diapir is sufficient to heat up the surrounding areas, the segregation can occur everywhere as in the case II.

The sinking diapir in Figs 1 and 2 belongs to dynamics which are closest to case IV. Its sinking velocity is a combination of the Stokes velocity of the dense iron diapir and a porosity wave phenomenon (akin to the magmon behaviour described, e.g. by Scott & Stevenson 1984), where the silicates traverse the metallic phase by a Darcy mechanism.

4.5 Energy transfer

As shown in eq. (14), the potential energy is converted into heat by three different mechanisms.

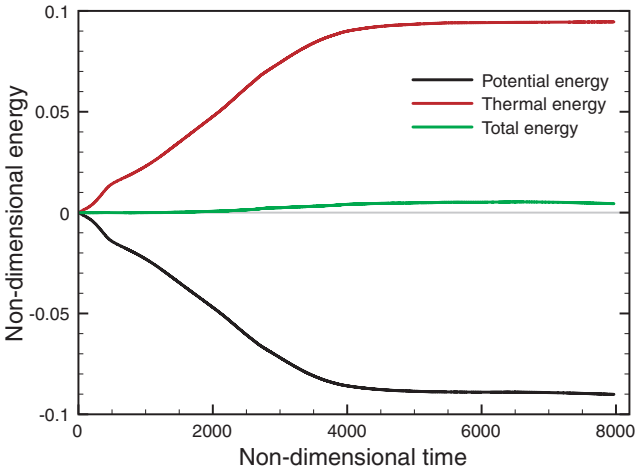

Figure 5. Energy conservation of the simulation presented in Section 4.2. The total energy (green curve) accumulates a relative error of at most 5 per cent of the potential energy change (black curve). Up to $t = 2000$ basically no error occurs. For $t > 2000$ the time stepping of the numerical code reaches an arbitrary minimum threshold (an accurate modelling of the extraction of the last bits of metal from silicates, where $\phi \sim 0$, or the last bits of silicates from metal, where $\phi \sim 1$, would require an extremely small time stepping) and we crudely impose a maximum porosity 0.995 and a minimum porosity 0.005. This is necessary to guarantee a reasonable execution time but decreases the accuracy of the results.

The usual viscous dissipation,

$$\mu^* \underline{\boldsymbol{\tau}}_m : \nabla \mathbf{v}_m, \tag{35}$$

the Darcy friction,

$$\frac{\Delta \mathbf{v}^2}{\delta^2}, \tag{36}$$

and the compaction,

$$\frac{1-\phi}{\phi}(\nabla \cdot \mathbf{v}_m)^2. \tag{37}$$

The sum of these three sources must balance exactly the decrease in gravitational energy (28). In the simulation shown previously (Figs 1 and 2), this global balance is satisfied as seen in Fig. 5. As the boundary of the computation domain is thermally insulated, the decrease in potential energy (black curve) corresponds to the increase of thermal energy (red curve). Their sum (green curve) remains equal to zero within machine accuracy up to $t \sim 2000$. As the differentiation proceeds and the metal content approaches locally 0, the removal of the last drops of metal (or reciprocally when the metal content reaches 1, the removal of the last silicates) becomes difficult. An accurate computation forces the time stepping to become very small and to reach the minimum time step that we impose for computational convenience. This results in a minor violation of the energy conservation that reaches at most 5 per cent of the total potential energy release.

Fig. 6 depicts the evolution of the three dissipation terms for the numerical simulation shown in Figs 1 and 2. Spatially averaged values are shown. The average heat sources are dominated either by the usual viscous dissipation (black curve) or by the Darcy dissipation term (green curve). The heat sources related to the compaction term are often negligible (red curve). However, occasionally, the three sources can have similar amplitudes locally. At times $t < 100$ the dissipation is dominated by the Darcy term which reflect the initial 1-D percolation within the impact zone. The peak

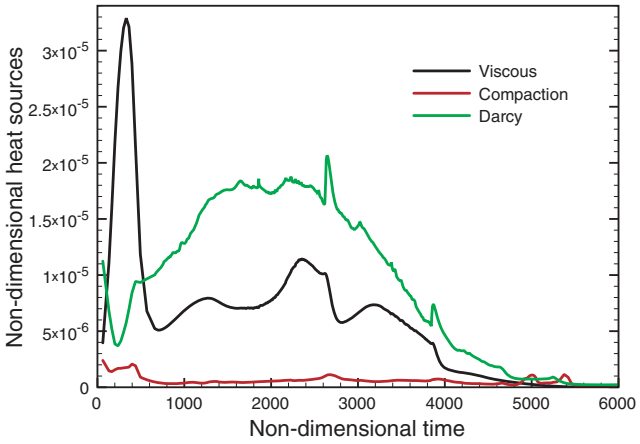

Figure 6. The three sources of dissipation occurring during the simulation shown in Fig. 1—viscous (eq. 35), Darcy (eq. 36) and compaction (eq. 37)—are spatially averaged and plotted as a function of time. Although locally and at a given time the three sources can have similar amplitudes, on average the dissipation is generally controlled by the Darcy term except during the travel through the undifferentiated mantle of large diapirs.

of viscous dissipation around $t = 330$ corresponds to the sinking of the large diapir. Of course as the segregation proceeds the rate at which the potential energy is converted to heat decreases and consequently the heat sources weaken. This is clearly visible at $t > 4000$ in Fig. 6 where all sources decline simultaneously, and where the global thermal and potential energies reach asymptotic values (± 0.094 for a fully segregated final state according to (26); Fig. 5).

4.6 Threshold of instability

Of course, the runaway destabilization of a proto-planet by an impact only occurs for a limited range of parameters. An impact on a planet that is too small or too cold may not provide enough energy to reach the metal melting temperature. A too small impactor may also increase the temperature in such a small domain that thermal diffusion will be faster than gravitational destabilization. Rather than trying to account for all the possible parameter variations, we focus on finding the conditions in which the runaway segregation instability develops, when the impactor size, the target planet's size and its background temperature are varied.

We ran a series of numerical experiments with the same setup as the simulation presented in Section 4.2. In a first set of experiments, the radius of the target planet is 2000 km (the impact heating ΔT is 258 K), and we investigate the post-impact evolution for different combinations of the initial temperature of the planet and the radius of the impact zone (which is proportional to the impactor radius, exceeding it by a factor of $f_2^{1/3} = 6^{1/3} \sim 1.8$). We monitor the melted/solid ratio of metal that we found either going to 0 or to 100 per cent in a few 100 kyr. The top panel of Fig. 7 (already presented in Ricard *et al.* 2009) shows several domains. If the initial temperature of the planet is below 1042 K, the melting temperature of metal T_{melt} is not reached and no segregation occurs (blue region). Obviously if the planet's initial temperature is above T_{melt} (1300 K), segregation occurs globally even without impact (yellow domain). For intermediate temperatures (1048–1300 K) the segregation is always initiated but the longer term evolution depends on the initial temperature and impact zone size. For large impactors (radius of impact zone normalized by planetary radius $\gtrsim 1/6$) only few K excess over the melting temperature in the impact zone is enough for

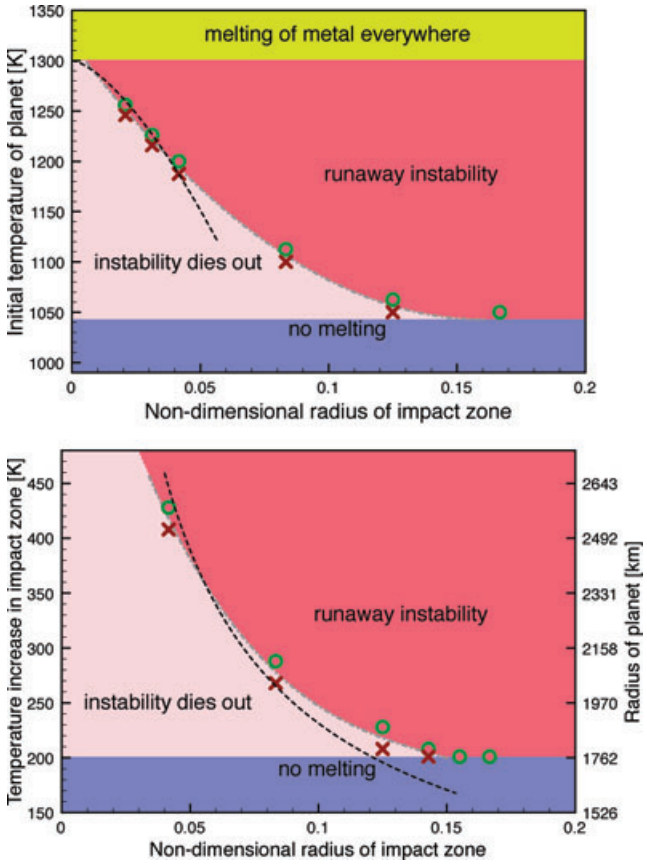

Figure 7. Regime diagram of the runaway instability. Numerical experiments were performed, where the normalized radius of the impact zone (therefore the impactor size), initial planetary temperature and planetary radius (and consequently the temperature increase in the impact zone) were varied. The top panel shows the threshold of instability in a cross section of the three-parameter space for fixed radius of the planet of 2000 km. The bottom panel shows a cross section for a fixed initial temperature of 1100 K. The numerical runs that constrain the threshold curves are shown by red crosses (instability dies out) and green circles (instability develops). The best fits to the analytical expressions are shown a black dashed lines.

the segregation instability to develop. When the impact zone radius is decreased, larger initial temperatures are required to overcome diffusion of heat out from the molten region. Some computation runs that constrain the threshold of instability are marked by red crosses (when the initially segregated metal, resolidifies) and green circles (when the initial metal sinking triggers further melting and segregation).

In a second set of experiments the initial temperature of the planet is 1100 K (200 K below $T_{\rm melt}$) and we vary the radius of the planet (hence the ΔT of the impact which varies as R^2) and the radius of the impact zone. The bottom panel of Fig. 7 summarizes the results. No melting occurs if the planet is too small ($R < 1762$ km) as in this case $\Delta T < 200$ K. Here again, for large impactors (impact zone radius $\gtrsim R/6$) the minimum ΔT for incipient melting is enough to trigger a large-scale instability. For smaller impactor sizes, the threshold ΔT increases when the normalized impact zone decreases.

The results of the numerical experiments, in particular the shape of the boundary between the runaway instability domain and the damping domain, can be supported by simple analysis. As was suggested, two competing effects operate. The metallic phase in the heated impact zone melts, segregates and sinks under its negative buoyancy. A characteristic advection timescale for the metallic diapir can be devised from the Stokes sinking velocity and the diapir radius R_d,

$$\tau_{\rm adv} \approx \frac{9\mu_m}{2\Delta\rho g R_d}. \tag{38}$$

Simultaneously with the sinking, temperature of the diapir decreases due to thermal diffusion. The maximum temperature at the centre of the spherical diapir evolves as $T_{\rm max} = T_0 + \Delta T\,{\rm erf}(R_d/\sqrt{4\kappa t})$. When the temperature drops below $T_{\rm melt}$, the metal freezes and the diapir propagation stops. We can estimate a freezing timescale, which is

$$\tau_{\rm freeze} \approx \frac{R_d^2}{4\kappa}\frac{\Delta T^2}{(T_{\rm melt}-T_0)^2} \tag{39}$$

for $(T_{\rm melt} - T_0)/\Delta T \ll 1$ (we used the fact that the error function is approximately linear for small values of its argument). The instability develops when the advection is much faster than the diffusion, that is, for $\tau_{\rm adv} \ll \tau_{\rm freeze}$,

$$\frac{\Delta\rho g R_d^3}{18\mu_m\kappa}\frac{\Delta T^2}{(T_{\rm melt}-T_0)^2} \equiv R_c \gg 1. \tag{40}$$

This reasoning is similar to the usual argument in simple convection, leading to the Rayleigh number; here the critical parameter is R_c. As the gravity g is proportional to the planetary radius R, ΔT is proportional to R^2 (see eq. 30) and the diapir radius R_d is proportional to the impact zone radius R_i (we write $R_d = f_3 R_i$ and f_3 is of order 1), from (38) and (39) we get the instability condition

$$\frac{R_i^3 R^5}{(T_{\rm melt}-T_0)^2} \gg A \equiv \left(\frac{3}{2}\right)^5 \frac{f_2^2}{\pi^3 f_1^2 f_3^3}\frac{\mu_m\kappa C}{G^3\overline{\rho}^3\Delta\rho}, \tag{41}$$

where A is a dimensional number independent of the planetary radius, the impact zone radius and the initial temperature. Consequently, for the first set of experiments in the top panel of Fig. 7 where we plot T_0 against R_i/R, we get an equation for the instability boundary

$$T_0 = T_{\rm melt} - a_1\left(\frac{R_i}{R}\right)^{\frac{3}{2}}, \tag{42}$$

where $a_1 = R^4/\sqrt{A}$ is a numerical constant. The numerically determined threshold curve indeed crosses the y-axis near $T_{\rm melt} = 1300$ K. As for the exponent, we obtain the value 1.1 if we consider the three points at high T_0 which conform to the assumption $(T_{\rm melt} - T_0)/\Delta T \ll 1$ of the above analysis. The best fit to the analytical expression (42) at high T_0 is shown as black dashed curve in Fig. 7. In the second set of experiments in the bottom panel of Fig. 7 the instability domain should be constrained by

$$R = a_2\left(\frac{R_i}{R}\right)^{-\frac{3}{8}}, \tag{43}$$

where $a_2 = (T_{\rm melt} - T_0)^{1/4} A^{1/8}$. The exponent obtained from the numerical experiments is 0.30, which is reasonably close to the analytical value of 0.375. The best fit to expression (43) is shown as black dashed curve in Fig. 7.

Notice that even rather small impactors are enough to trigger a complete and rapid metal segregation provided that the planet is large enough and/or the initial temperature is sufficiently close to the melting point of metal. As both the initial energy thermal deposition by the impact and the gravitational energy release associated with segregation vary with the square of the proto-planetary radius, this runaway core formation seems inescapable in growing planets unless the population of impactors drifts to very small sizes.

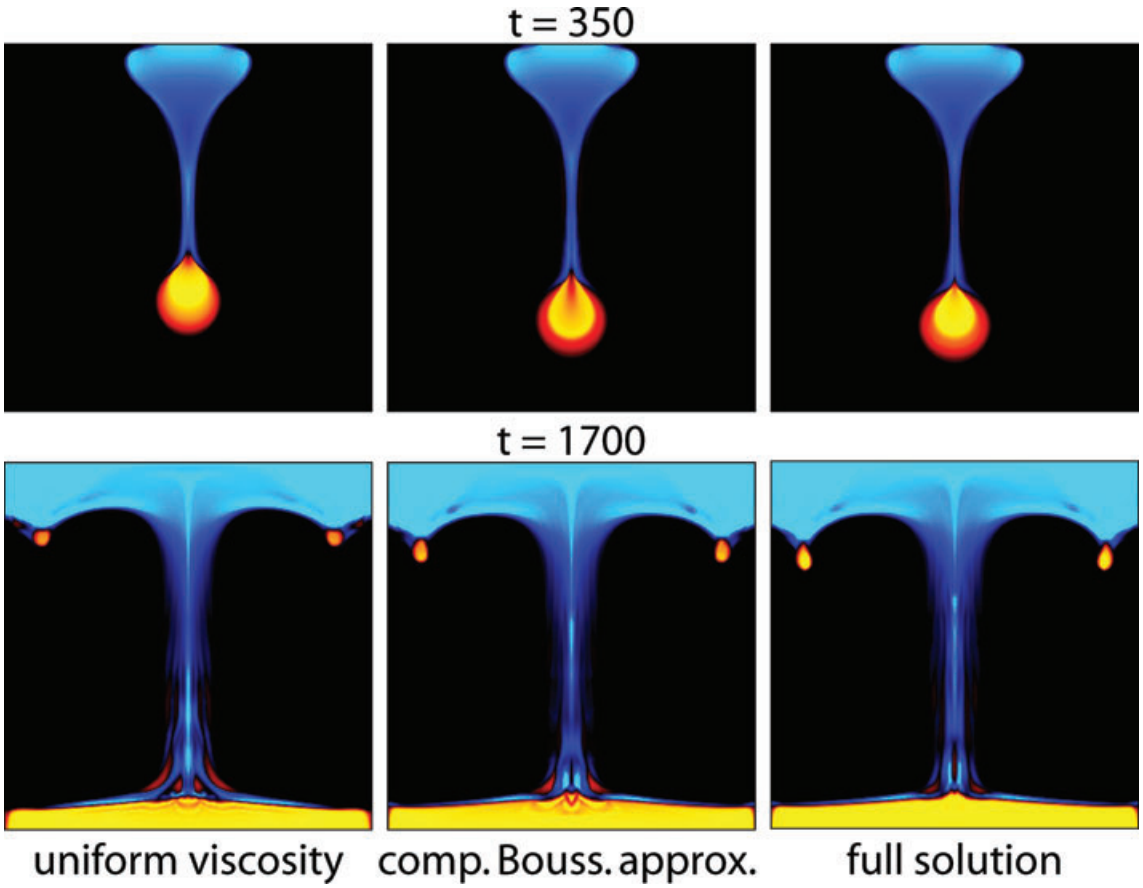

Figure 8. Metal volume fraction at $t = 350$ (first row) and $t = 1700$ (second row). Left-hand column: the viscosity is assumed uniform, independent of the liquid metal content. Middle column: compaction Boussinesq approximation, the irrotational components of the velocity are computed with variable viscosity but a uniform viscosity is assumed for the compressible flow. Right-hand column: full solution. The initial condition is identical in the three simulations. Colour scale is the same as in Figs 1 and 9.

4.7 Full and approximate solutions

The simulations previously discussed have been computed in the compaction Boussinesq approximation (Schmeling 2000). The time necessary for a simulation increases more or less by one order of magnitude when we implement this approximation rather than the crudest approximation of uniform viscosity. Another order of magnitude in time duration is needed to compute the full solution. Accounting for porosity-dependent viscosity variations (full solution) somewhat increases the velocities with respect to the uniform viscosity case. The differences between the three computations remain however small (less than 10 per cent) and do not seem to justify the time spent for the full solution. The sinking velocity of diapirs is mostly controlled by the high viscosity of the surrounding solid phase. This is similar to what happens for the sinking velocity of a sphere in a viscous medium: according to the Rybczynski–Hadamard solutions (see e.g. Ribe 2007) an inviscid sphere only falls 1.5 times faster than a solid sphere. The velocity of the fluid phase computed by the Darcy equation seems also very weakly dependent on the level of approximation performed in computing the pressure field.

In Fig. 8, we show three computations of the initial sinking of a diapir at the same time, but performed with a uniform viscosity (left-hand panel), the compaction Boussinesq approximation (middle panel) or the full solution (right-hand panel). Accounting for the decrease in viscosity proportional to the melt fraction increases the sinking velocity of the first diapirs. The full solution is also slightly faster than the compaction Boussinesq case. However except for minor details the solutions remain very similar. Of course a stronger dependence of viscosity with metal content (like in Golabek *et al.* 2008) may require an exact computation. To be able to run various simulations in a reasonable amount of time, we generally use the compaction Boussinesq approximation.

4.8 Initial conditions and geometry

The simulations discussed so far were confined to a square box and assumed an initial uniform distribution of metal. Such an idealized initial condition may not correspond to the real situation. The planetesimals that impacted on the growing planet may have been partially differentiated because of heating by short-lived radionuclides and subsequent metal sinking by permeable flow (Yoshino *et al.* 2003). It is difficult to constrain a realistic initial condition for our model. The distribution of metal and thermal state of the growing planet reflects an integrated history of previous impacts and possible internal dynamical evolution. The length scale of metal–silicate-rich heterogeneities in the growing planet is controlled by the degree of differentiation of arriving impactors, by the degree of their fragmentation and remixing upon impact, as well as by the size of impactors. The composition of impacting planetesimals probably spanned a wide range between undifferentiated to largely

differentiated bodies. The average size of impactors increases with time during planetary accretion. It is reasonable to assume that the characteristic size of inhomogeneities in metal–silicate distribution in the target planet was smaller than the extent of the impact zone of the latest impactor.

We computed an additional model where the initial metal concentration is random in each cell with exponential distribution and mean value of 0.25 (same as in the previous cases). This grid size heterogeneity represents variation on 10 km scale. Clearly, a spherical geometry would be better suited for a planetary core segregation study. At present however, our code is implemented only in Cartesian geometry. To imitate the ratio of near-surface circumference to radius for a sphere, we compute this additional model in a Cartesian box of a large aspect ratio 3. Images of metal fraction are shown in Fig. 9 (a smaller version of this figure was presented in Ricard *et al.* 2009). The progression and outcome of this model are very similar to the case with uniform initial metal fraction (Fig. 1), although the total duration of the segregation is increased by a factor ∼2. The first large diapir originates in the impact zone and sinks to the bottom. Subsequent diapirs advance the segregation as the differentiated metal and silicates spread along the bottom and top panels, respectively. The last region to undergo differentiation is the deepest mantle. The initial random concentration results in patterns that are no longer symmetric about the vertical mid-axis.

Various complexities of 3-D flow and spherical geometry are necessarily poorly scaled in 2-D model. For example, the 2-D assumption of uniform gravity overestimates the heat release by gravitational settling by ∼70 per cent – the equivalent of eq. (32) in Cartesian coordinates and a uniform gravity is $\Delta E_2 = \Delta\rho g_0 R\phi_0(1-\phi_0)/(2\overline{\rho})$. However assuming that gravity varies linearly with depth would underestimate ΔE_2 by ∼30 per cent. To obtain the same potential energy release in 2-D as in 3-D (see 32) we can use a gravity varying as $\hat{g} = z^{0.567}$ (z is the normalized height). The numerical simulations using $\hat{g} = 1, \hat{g} = z^{0.567}$, and $\hat{g} = z$ are depicted in Fig. 10. In these simulations, we assume an initial heterogeneous metal concentration.

The left-hand column (uniform gravity) is very similar to the results depicted in Fig. 1 (the only difference is an initial heterogeneous composition). As expected the segregation process slows down when the gravity is zero at the centre (middle and right-hand

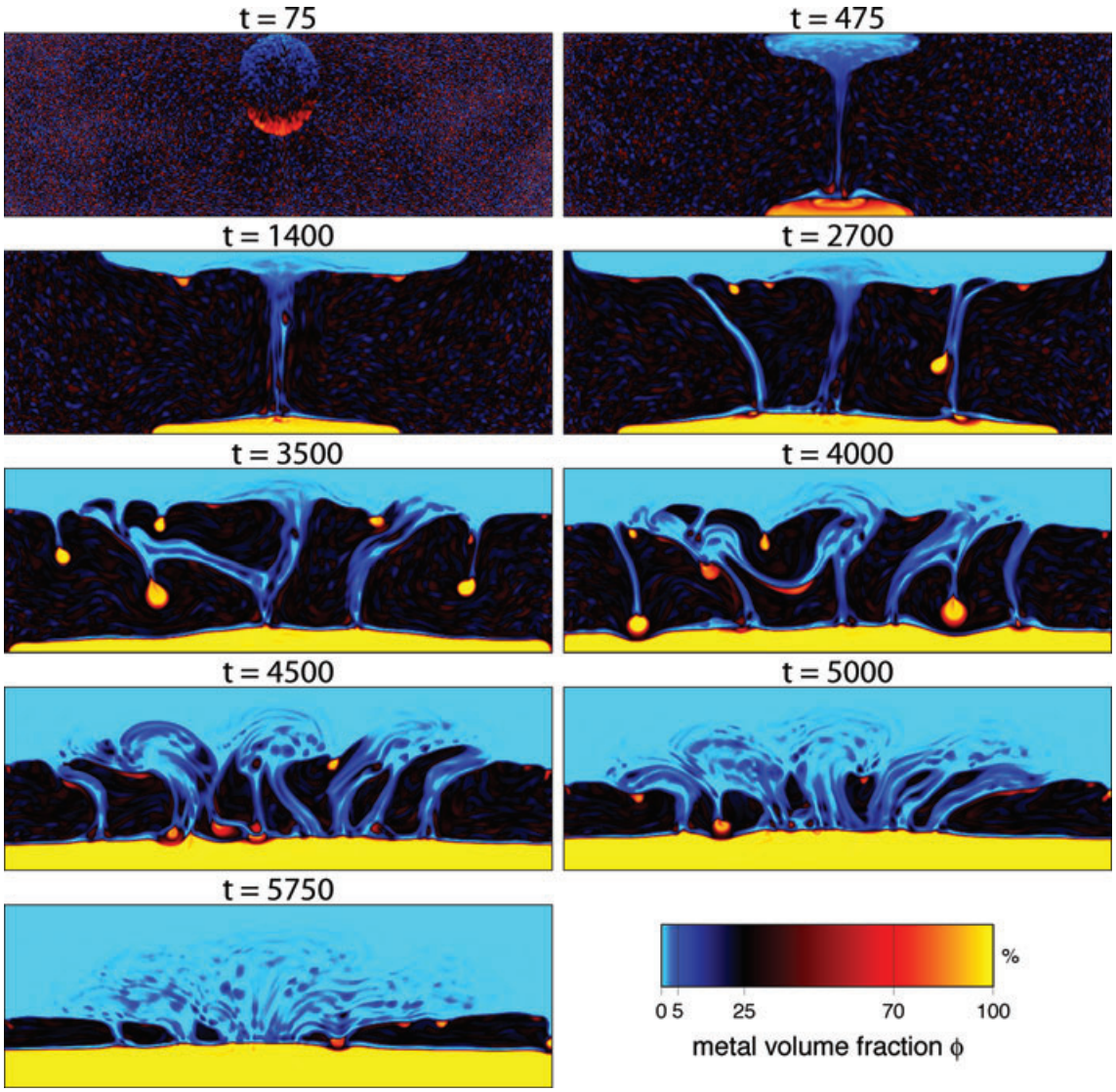

Figure 9. Evolution of the metal volume fraction in a rectangular box of aspect ratio 3 with a random initial composition. The impact zone radius is 1/4 of the box depth. The normalized times are indicated. The compaction Boussinesq approximation is used on a regular grid with 600 × 200 grid cells.

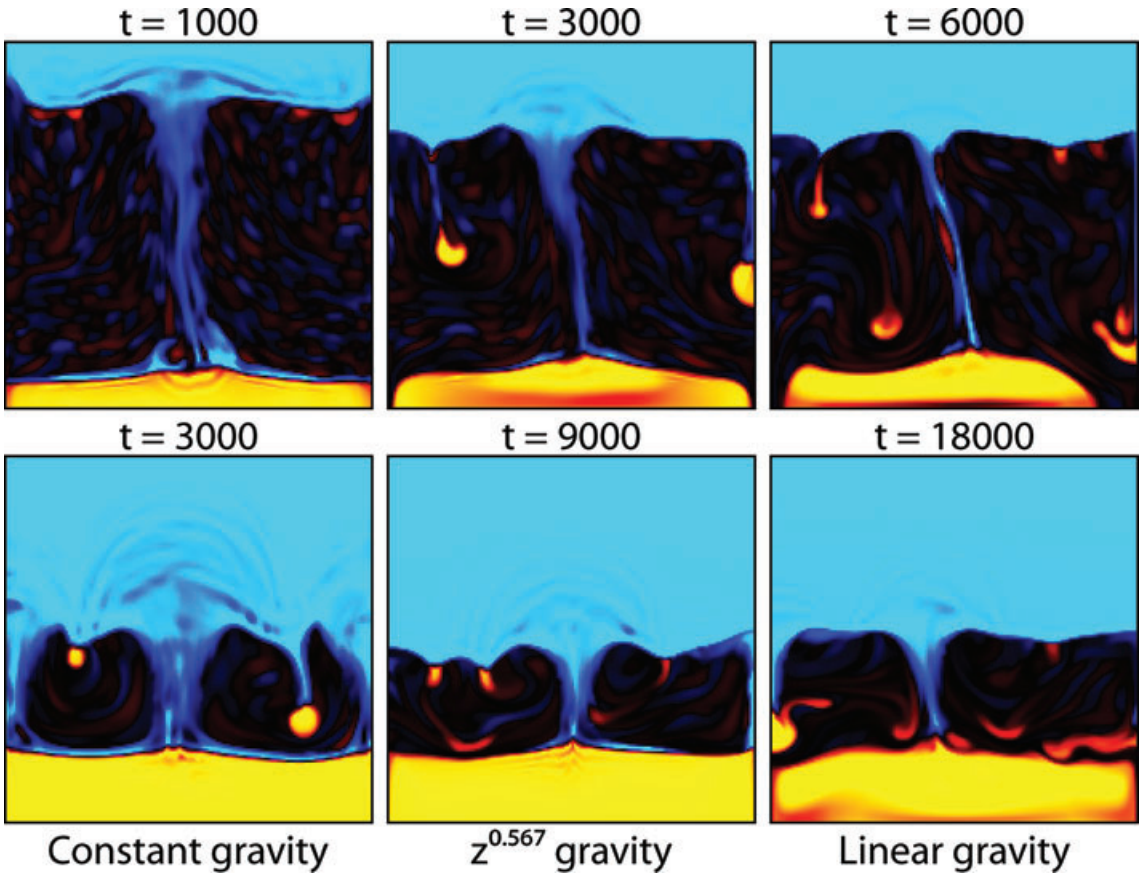

Figure 10. Metal volume fraction during segregation when the gravity is assumed constant (left-hand column), varies like $z^{0.567}$ (middle column) or like z (left-hand column). We assume a random initial composition. In the middle column, the energy release is similar to what would be released in a spherical planet. The evolution is very similar to the case with constant gravity (left-hand column) when the time is multiplied by 3 (middle column) and 6 (right-hand column). The complete segregation occurs for the three cases in ∼6, ∼18 and ∼24 kyr.

columns). Metal-rich zones tend to stagnate in the deep mantle (right-hand column). However even if we use a gravity that increases linearly from zero at the bottom of the box (right-hand column), we still observe the same runaway segregation. The gravitational energy release is even then sufficient to eventually melt all the metal (with the caveat of neglected latent heat of fusion). The main difference is an increased differentiation timescale by factors of ∼3 ($\hat{g} = z^{0.567}$, middle column) or ∼6 ($\hat{g} = z$, right-hand column).

In all these simulations, we do not account for the temporal change of gravity due to mass redistribution. In fact, as the differentiation proceeds in a real planetesimal, the central region becomes progressively denser compared to the upper layers. This results in the gravity magnitude increasing more rapidly from the centre outwards than a linear increase for a uniform density body and also increasing with time, and therefore enhances buoyancy. A more realistic model of core formation would require solving our proposed equations in 3-D spherical geometry. The thermomechanical equations would need to be coupled to a Poisson equation solving for the gravity potential, as the redistribution of large masses during the segregation results in non-uniform and constantly evolving gravity.

4.9 Rayleigh number and compaction length

In the reference calculation we have used a Rayleigh number $Ra = 10^6$ rather than 10^{10} which corresponds to the chosen parameters (Table 1). It effectively translates into using thermal diffusivity four orders of magnitude larger than the reference value (see eq. 14). We used a smaller Rayleigh number to insure numerical stability of the advection-diffusion equation for temperature. In Fig. 11, we show a simulation where the Rayleigh number has been increased to 10^8. This is the highest limit to which we may trust the accuracy of our code.

Increasing the Rayleigh number reduces, as expected, the volume of the metallic diapirs and increases their number. It somewhat slows down the differentiation because the thermal diffusion is less effective in bringing up the temperature above the melting point in regions adjacent to the already differentiated parts. The complete differentiation timescale increases roughly by a factor of ∼2 for this two orders of magnitude increase in Ra, but the overall dynamics remain unchanged.

We have also explored the dependence of the dynamics on the value of the compaction length (see Fig. 12). We have varied δ^2 between 10^{-3} (left-hand column) and 10^{-1} (right-hand column), that is, a two orders of magnitude variation in μ_m/μ_f; the reference case described in Section 4.2 was calculated with $\delta^2 = 10^{-2}$ ($\delta = 0.1$). For cases with $\delta \gtrsim 0.1$ (right-hand column) we observe an evolution very similar to our reference case. The trailing channels widen and the characteristic non-dimensional time of segregation decreases roughly as $\delta^{-1/2}$. For small compaction lengths, $\delta^2 = 10^{-3}$ (left-hand column), as the segregation controlled by matrix compaction becomes less effective at global spatial scale, the picture changes from the one with small number of dominant iron-rich diapirs to one with a larger number of weaker iron rich downwellings and iron-depleted upwellings. As the compaction length is reduced,

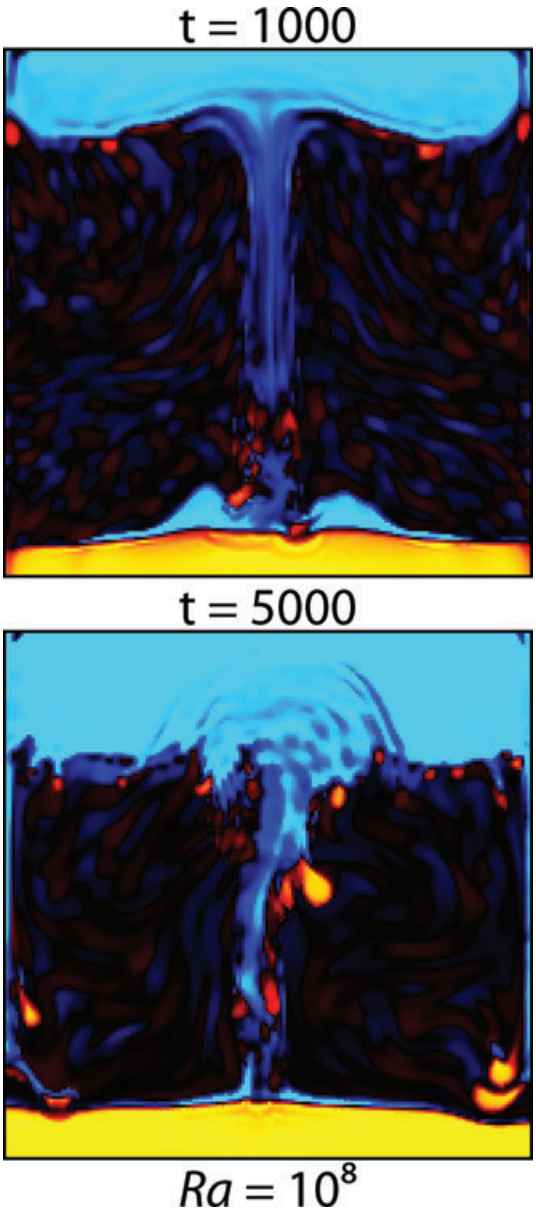

Figure 11. Metal volume fraction during segregation with $Ra = 10^8$. A comparison with Fig. 10 (left-hand column) where $Ra = 10^6$ shows that the increase of the Rayleigh number decreases the volume of the metallic diapirs and increases the segregation time.

the non-dimensionalized differentiation timescale increases rapidly. The complete extraction of metal from silicates becomes difficult. There is most probably a threshold in δ below which the initial instability dies out completely as the separation of metal from silicate in the impacted zone becomes impossible.

Some caution is needed to translate the non-dimensional numbers into dimensional parameters and time constraints. For example, a change in the non-dimensional compaction length can be due to a change in μ_m or to a change in μ_f. The former also affects the time scaling and the Rayleigh number.

5 DISCUSSION AND CONCLUSION

Up to now, the models of core mantle segregation by near-surface partial melting followed by the destabilization of metallic diapirs were often advocated but only illustrated by cartoons. To our knowledge, our model is the first one to attempt a fluid dynamic modelling with the complexities inherent to the problem: its multiphase nature, the irrelevance of the standard Boussinesq approximation, and the necessity to account for the energy conversion between gravitational and thermal energies.

Our modelling however, includes some important simplifying assumptions that must be discussed. First, we have neglected the latent heat during metal phase change. This has greatly simplified the formalism as the knowledge of temperature alone has been sufficient to determine the proportion of liquid. If the latent heat were properly accounted for, the instability would evolve at a somewhat slower pace; upon reaching the iron melting temperature at a material point, the proportion of liquid iron would gradually increase from zero at a rate proportional to the rate of gravitational energy release, rather than changing from zero to maximum instantaneously. In consequence, latent heat would somewhat moderate the increase in temperature; the curved regime boundaries in Fig. 7 would be displaced towards the 'runaway instability' region. Nevertheless, as the average temperature in the planet at the end of the presented simulation is well above the iron melting temperature (by ∼225 K), even the latent heat buffering should not change significantly the general evolution. As the core alloy melts at a temperature much lower than the pure iron, it is also likely that its latent heat should be significantly lower than that of the pure metal that we considered in numerical applications.

Second, we have used the same Darcy interaction formalism at all metal fractions. This assumes that both the molten metal and the solid phase remain interconnected at all metal fractions. However, in reality, when the volume fraction of liquid metal reaches few tens of percent, the mixture should rather resemble a slurry of solid grains suspended in the molten metal. To account for this accelerated separation at high metal fraction, an interaction parameter c (or equivalently permeability) with more complex metal proportion dependence based on laboratory experiments could be implemented.

Third, we have used a porosity dependent viscosity for the silicates–molten metal mixture of the form $\mu^* = 1 - \phi$. This is a much weaker porosity dependence than is obtained in experimental studies on deformation of partially molten rock samples, where the data is fitted to $\mu^* \propto \exp(-\alpha\phi)$ dependence (Zimmerman & Kohlstedt 2004; Scott & Kohlstedt 2006; Hustoft *et al.* 2007). For olivine plus metallic melt the experiments of Hustoft *et al.* (2007) yield $\alpha = 4$. These experiments where performed up to porosity 0.2 at a relatively low pressure (300 MPa), where the dihedral angle of the metallic melt exceeds 90°. It is possible that as the dihedral angle drops below 90° at high pressure, the exponent may become even larger. One may argue that the exponential $\mu^*(\phi)$ dependence should be used in the modelling. However, there is no reason why this empirical law should be valid at all porosities. In fact, as discussed above, a very crude approximation is the mere use of the same Darcy flow formalism at all porosities, which does not capture the change of the physical mechanism when the originally interconnected solid framework disaggregates into a suspension of grains in liquid. With a linear $\mu^*(\phi)$ dependence we circumvent the need for a Stokes problem solver capable of handling large viscosity contrasts. A stronger porosity dependence would bring no new physics into the model; it would obviously result into quantitative changes, such as reducing the already quite short timescale of segregation. Results of our calculations with varied Rayleigh number or compaction length suggest that the change in timescale would only be moderate.

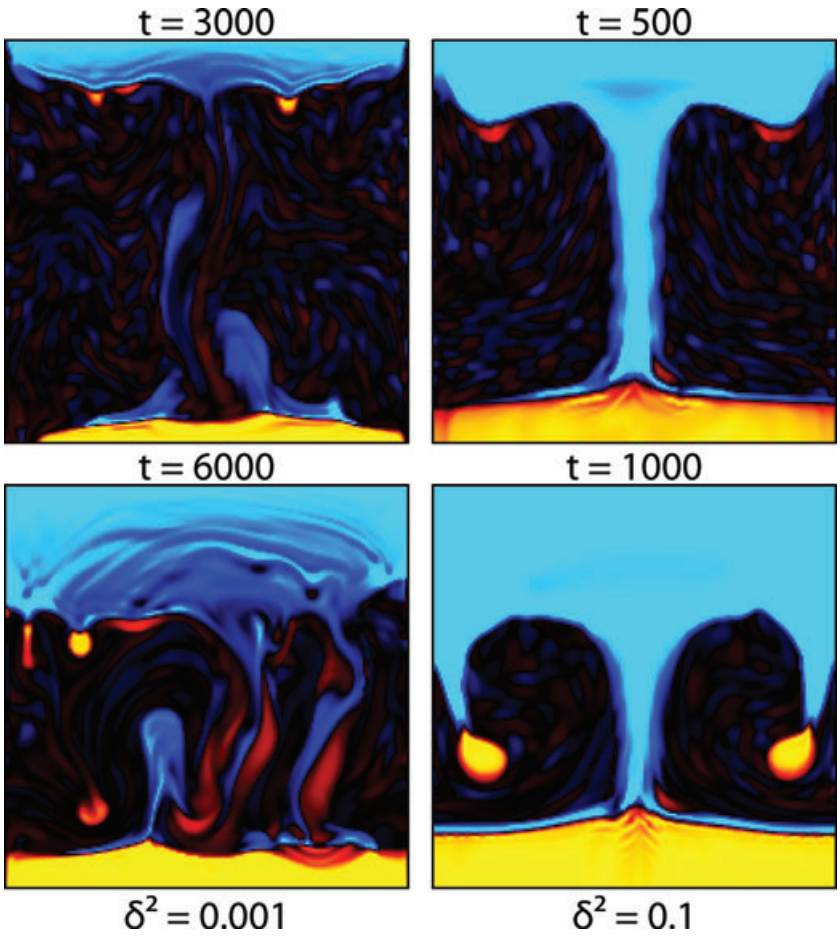

Figure 12. Metal volume fraction during segregation with $\delta^2 = 0.001$ (left-hand column) and $\delta^2 = 0.1$ (right-hand column). This Figure can be compared with Fig. 10 (left-hand column) where $\delta^2 = 0.01$. A decrease of the compaction length favours the upwelling of light silicate diapirs from the proto-core boundary (left-hand column).

The fundamental ingredient of the runaway core formation predicted by our model is the same R^2-dependence of both the thermal energy deposition in the impact zone of a meteoric impact and the gravitational energy release upon segregation, and their similar magnitude. As soon as this energy reaches a few hundred kJ kg^{-1} (an equivalent temperature increase of few hundred degrees) for a growing proto-planet, which occurs at $R \gtrsim 1500$ km, rapid core formation should occur within a few tens of thousand years. This segregation cannot be delayed much longer as at some point the R^2-dependent impact heating will bring the planetary temperature close to the iron melting point. Although the extrapolation of the 2-D modelling results to 3-D spherical planet are difficult, we have observed that even small impacts (see Fig. 7) suffice to trigger the core-forming instability.

The process of core formation predicted by our model is significantly different from the usual cartoons (e.g. Stevenson 1990; Righter 2003). The first diapir that crosses the mantle leaves a cusp-like trailing conduit that connects the proto-core to the near surface silicates across the undifferentiated material. Melting occurs continuously both in the shallow and in the deep mantle. The highest temperatures are reached in the conduit itself. The release of gravitational energy increases the temperature both in the proto-core and the shallow silicate mantle, and leaves the deep undifferentiated mantle rather cold. The sinking of metallic diapirs is very fast (of order of 10 kyr). Instead of the diapir having to deform the surrounding material as in a usual Stokes flow, the undifferentiated material phases separate on the bottom side of the diapir, the silicates cross the metallic phase, and accumulate behind the sinking diapir. The motion of the diapir thus involves both the porosity wave and the usual Stokes flow.

The timescale we obtain from our model, for example, a proto-core formation in ∼110 kyr, obviously depends on the values of the material parameters that control both the characteristic scales and the dimensionless parameters in the equation. The largest uncertainties in parameter values are carried by the viscosities. Both the timescale τ used for non-dimensionalization and the Rayleigh number depend on the solid viscosity ($\tau \propto \mu_m$, $Ra \propto \mu_m^{-1}$), while the square of the non-dimensionalized compaction length is proportional to the solid to liquid viscosity ratio ($\delta^2 \propto \mu_m/\mu_f$). An order of magnitude variation in solid viscosity translates into an equal variation of the timescale. A longer/shorter compaction length means a faster/slower Darcy separation and affects the overall evolution in a non-trivial manner. Taking into account the overall large number of parameters, we have certainly not sampled the whole parameter space. At any rate, the very large density loads, the high temperature, and the presence of a liquid phase all point to a fast dynamics.

The potential inferences on the Earth's core or mantle chemistry, for example, the temperature of equilibration of various components, that could be made from our modelling are limited by the fact that we predict the proto-core formation in an early stage of

planetary evolution where the proto-core mass is only a few percent of that of the present-day Earth (because of the small radius of the proto-planet and much higher density of the high-pressure phases in a large planet's core). Therefore most of the core mass of a large differentiated planet was added after the situation described in this paper by the still ongoing accretion of planetesimals.

ACKNOWLEDGMENTS

We thank John Hernlund and Richard Katz for their thoughtful reviews and suggestions that improved the manuscript. Fruitful discussions with Nicolas Coltice and Stéphane Labrosse benefited this paper. The work was supported by the ANR ETHER.

REFERENCES

Agee, C.B., Li, J., Shannon, M.C. & Circone, S., 1995. Pressure-temperature phase diagram for the Allende meteorite, *J. geophys. Res.,* **100**(B9), 17 725–17 740.

Batchelor, G.K., 1967. *An Introduction to Fluid Dynamics,* Cambridge University Press, Cambridge.

Bear, J., 1988. *Dynamics of Fluids in Porous Media,* Dover Publications, New York, NY.

Benz, W. & Cameron, A.G.W., 1990. Terrestrial effects of the giant impact, in *Origin of the Earth,* pp. 61–67, eds Newsom, H.E. & Jones, J.H., Oxford University Press, New York, NY.

Bercovici, D. & Ricard, Y., 2003. Energetics of a two-phase model of lithospheric damage, shear localization and plate boundary formation, *Geophys. J. Int.,* **152**(3), 581–596.

Bercovici, D., Ricard, Y. & Schubert, G., 2001. A two-phase model for compaction and damage. Part 1: general theory, *J. geophys. Res.,* **106**(B5), 8887–8906.

Boehler, R., 1996. Experimental constraints on melting conditions relevant to core formation, *Geochim. Cosmochim. Acta,* **60**(7), 1109–1112.

Canup, R.M. & Asphaug, E., 2001. Origin of the Moon in a giant impact near the end of the Earth's formation, *Nature,* **412**(6848), 708–712.

Carlson, R.W. & Langmuir, G.W., 2000. Timescales of planetesimal formation and differenciation based on extinct and extant radioisotopes, in *Origin of the Earth and Moon,* pp. 25–44, eds Canup, R.M. & Righter, K., University of Arizona Press, Tucson, AZ.

Davies, G.F., 1980. Exploratory models of the Earth's thermal regime during segregation of the core, *J. geophys. Res.,* **85**(B12), 7108–7114.

Fei, Y., Bertka, C.M. & Finger, L.W., 1997. High-pressure iron-sulfur compound, Fe_3S_2, and melting relations in the Fe-FeS system, *Science,* **275**(5306), 1621–1623.

Flasar, F.M. & Birch, F., 1973. Energetics of core formation: a correction, *J. geophys. Res.,* **78**(26), 6101–6103.

Gerya, T.V. & Yuen, D.A., 2007. Robust characteristics method for modelling multiphase visco-elastic thermo-mechanical problems, *Phys. Earth planet. Int.,* **163**(1–4), 83–105.

Golabek, G.J., Schmeling, H. & Tackley, P.J., 2008. Earth's core formation aided by flow channelling instabilities induced by iron diapirs, *Earth planet. Sci. Lett.,* **271**(1–4), 24–33.

Greenwood, R.C., Franchi, I.A., Jambon, A. & Buchanan, P.C., 2005. Widespread magma oceans on asteroidal bodies in the early Solar System, *Nature,* **435**(7044), 916–918.

Harten, A., 1983. High resolution schemes for hyperbolic conservation laws, *J. Comp. Phys.,* **49**(3), 357–393.

Hernlund, J.W. & Tackley, P.J., 2007. Some dynamical consequences of partial melting in Earth's deep mantle, *Phys. Earth planet. Int.,* **162**(1–2), 149–163.

Hewitt, J.M., McKenzie, D.P. & Weiss, N.O., 1975. Dissipative heating in convective flows, *J. Fluid Mech.,* **68**(4), 721–738.

Hier-Majumder, S., Ricard, Y. & Bercovici, D., 2006. Role of grain boundaries in magma migration and storage, *Earth planet. Sci. Lett.,* **248**(3–4), 735–749.

Hirschmann, M.M., 2000. Mantle solidus: experimental constraints and the effects of peridotite composition, *Geochem. Geophys. Geosyst.,* **1**(10), doi:10.1029/2000GC000070.

Höink, T., Schmalzl, J. & Hansen, U., 2006. Dynamics of metal-silicate separation in a terrestrial magma ocean, *Geochem. Geophys. Geosyst.,* **7**(9), Q09008, doi:10.1029/2006GC001268.

Honda, R., Mizutani, H. & Yamamoto, T., 1993. Numerical simulation of Earth's core formation, *J. geophys. Res.,* **98**(B2), 2075–2089.

Hustoft, J., Scott, T. & Kohlstedt, D.L., 2007. Effect of metallic melt on the viscosity of peridotite, *Earth planet. Sci. Lett.,* **260**(1–2), 355–360.

Karato, S. & Murthy, V.R., 1997. Core formation and chemical equilibrium in the Earth–I. Physical considerations, *Phys. Earth planet. Int.,* **100**(1–4), 61–79.

Katz, R.F., 2008. Magma dynamics with the enthalpy method: benchmark solutions and magmatic focusing at mid-ocean ridges, *J. Petrol.,* **49**(12), 2099–2121.

Katz, R.F., Knepley, M.G., Smith, B., Spiegelman, M. & Coon, E.T., 2007. Numerical simulation of geodynamic processes with the Portable Extensible Toolkit for Scientific Computation, *Phys. Earth planet. Int.,* **163**(1–4), 52–68.

Kaula, W.M., 1979. Thermal evolution of Earth and Moon growing by planetisimal impacts, *J. geophys. Res.,* **84**(NB3), 999–1008.

Kelemen, P.B., Hirth, G., Shimizu, N., Spiegelman, M. & Dick, H.J.B., 1997. A review of melt migration processes in the adiabatically upwelling mantle beneath oceanic spreading ridges, *Phil. Trans. R. Soc. Lond. A,* **355**(1723), 283–318.

Kleine, T., Münker, C., Mezger, K. & Palme, H., 2002. Rapid accretion and early core formation on asteroids and the terrestrial planets from Hf–W chronometry, *Nature,* **418**(6901), 952–955.

Kleine, T., Mezger, K., Palme, H. & Munker, C., 2004. The W isotope evolution of the bulk silicate Earth: constraints on the timing and mechanisms of core formation and accretion, *Earth planet. Sci. Lett.,* **228**(1-2), 109–123.

Laney, C.B., 1998. *Computational Gasdynamics,* Cambridge University Press, Cambridge.

Leveque, R.J., 1996. High-resolution conservative algorithms for advection in incompressible flow, *SIAM J. Numer. Anal.,* **33**(2), 627–665.

Li, J. & Agee, C.B., 1996. Geochemistry of mantle-core differentiation at high pressure, *Nature,* **381**(6584), 686–689.

Matsui, T. & Abe, Y., 1986a. Formation of a 'magma ocean' on the terrestrial planets due to the blanketing effect of an impact-induced atmosphere, *Earth, Moon Planets,* **34**(3), 223–230.

Matsui, T. & Abe, Y., 1986b. Impact-induced atmospheres and oceans on Earth and Venus, *Nature,* **311**(6079), 526–528.

McKenzie, D., 1984. The generation and compaction of partially molten rock, *J. Petrol.,* **25**(3), 713–765.

Melosh, H.J., 1996. *Impact Cratering: A Geologic Process,* Oxford University Press, New York, NY.

Monteux, J., Coltice, N., Dubuffet, F. & Ricard, Y., 2007. Thermo-mechanical adjustment after impacts during planetary growth, *Geophys. Res. Lett.,* **34,** L24201.

Monteux, J., Ricard, Y., Coltice, N., Dubuffet, F. & Ulvrova, M., 2009. A model of metal-silicate separation on growing planets, *Earth planet. Sci. Lett.,* **287**(3–4), 353–362.

Nimmo, F. & Agnor, C.B., 2006. Isotopic outcomes of N-body accretion simulations: constraints on equilibration processes during large impacts from Hf/W observations, *Earth planet. Sci. Lett.,* **243**(1–2), 26–43.

O'Keefe, J.D. & Ahrens, T.J., 1999. Complex craters: relationship of stratigraphy and rings to impact conditions, *J. geophys. Res.,* **104**(E11), 27 091–27 104.

Olson, P. & Weeraratne, D., 2008. Experiments on metal–silicate plumes and core formation, *Phil. Trans. R. Soc. Lond. A,* **366**(1883), 4253–4271.

Patankar, S.V., 1980. *Numerical Heat Transfer And Fluid Flow,* Vol.8: Computational and Physical Processes in Mechanics and Thermal Sciences, Taylor & Francis, London.

Pierazzo, E., Vickery, A.M. & Melosh, H.J., 1997. A reevaluation of impact melt production, *Icarus,* **127**(2), 408–423.

Pietrzak, J., 1998. The use of TVD limiters for forward-in-time upstream-biased advection schemes in ocean modeling, *Mon. Wea. Rev.,* **126**(3), 812–830.

Rabinowicz, M., Genthon, P., Ceuleneer, G. & Hillairet, M., 2001. Compaction in a mantle mush with high melt concentrations and the generation of magma chambers, *Earth planet. Sci. Lett.,* **188**(3–4), 313–328.

Ribe, N.M., 2007. Analytical approaches to mantle dynamics, in *Mantle Dynamics,* Vol. 7, chap. 7.04, pp. 167–226, eds Gerald, S. & Bercovici, D., Treatise on Geophysics, Elsevier Scientific Publishing Company, New York.

Ricard, Y., 2007. Physics of mantle convection, in *Mantle Dynamics,* Vol. 7, Chap. 7.02, pp. 31–87, eds Gerald, S. & Bercovici, D., Treatise on Geophysics, Elsevier Scientific Publishing Company, New York.

Ricard, Y., Šrámek, O. & Dubuffet, F., 2009. A multi-phase model of runaway core-mantle segregation in planetary embryos, *Earth planet. Sci. Lett.,* **284**(1-2), 144–150.

Richter, F.M. & McKenzie, D., 1984. Dynamical models for melt segregation from a deformable matrix, *J. Geol.,* **92**(6), 729–740.

Righter, K., 2003. Metal-silicate partitioning of siderophile elements and core formation in the early Earth, *Annu. Rev. Earth planet. Sci.,* **31,** 135–174.

Roe, P.L., 1985. Some contributions to the modelling of discontinuous flows, in *Large-Scale Computations in Fluid Mechanics; Proceedings of the Fifteenth Summer Seminar on Applied Mathematics, La Jolla, CA,* pp. 163–193, American Mathematical Society, Providence, RI.

Rubie, D.C., Melosh, H.J., Reid, J.E., Liebske, C. & Righter, K., 2003. Mechanisms of metal-silicate equilibration in the terrestrial magma ocean, *Earth planet. Sci. Lett.,* **205**(3–4), 239–255.

Rushmer, T., Minarik, W.G. & Taylor, G.J., 2000. Physical processes of core formation, in *Origin of the Earth and Moon,* pp. 25–44, eds Canup, R.M. & Righter, K., University of Arizona Press, Tucson, AZ.

Samuel, H. & Tackley, P.J., 2008. Dynamics of core formation and equilibrium by negative diapirism, *Geochem. Geophys. Geosyst.,* **9,** Q06011, doi:10.1029/2007GC001896.

Schmeling, H., 2000. Partial melting and melt segregation in a convecting mantle, in *Physics and Chemistry of Partially Molten Rocks,* Vol. 11, Chap. 5, pp. 141–178, eds Bagdassarov, N., Laporte, D. & Thompson, A.B., Petrology and Structural Geology, Kluwer Academic Publisher, Dordrecht.

Scott, D.R. & Stevenson, D.J., 1984. Magma solitons, *Geophys. Res. Lett.,* **11**(11), 1161–1164.

Scott, T. & Kohlstedt, D.L., 2006. The effect of large melt fraction on the deformation behavior of peridotite, *Earth planet. Sci. Lett.,* **246**(3–4), 177–187.

Senshu, H., Kuramoto, K. & Matsui, T., 2002. Thermal evolution of a growing Mars, *J. geophys. Res.,* **107**(E12), 5118.

Smolarkiewicz, P.K., 1983. A simple positive definite advection scheme with small implicit diffusion, *Mon. Wea. Rev.,* **111**(3), 479–486.

Solomatov, V.S., 2000. Fluid dynamics of a terrestrial magma ocean, in *Origin of the Earth and Moon,* pp. 323–338, eds Canup, R.M. & Righter, K., University of Arizona Press, Tucson, AZ.

Solomon, S.C., 1979. Formation, history and energetics of cores in the terrestrial planets, *Phys. Earth planet. Int.,* **19**(2), 168–182.

Spiegelman, M., 1993. Physics of melt extraction: theory, implications and applications, *Trans. R. Soc. Lond. A,* **342**(1663), 23–41.

Spiegelman, M. & McKenzie, D., 1987. Simple 2-D models for melt extraction at mid-ocean ridges and island arcs, *Earth planet. Sci. Lett.,* **83**(1–4), 137–152.

Šrámek, O., Ricard, Y. & Bercovici, D., 2007. Simultaneous melting and compaction in deformable two-phase media, *Geophys. J. Int.,* **168**(3), 964–982.

Stevenson, D.J., 1990. Fluid dynamics of core formation, in *Origin of the Earth,* pp. 231–249, eds Newsom, H.E. & Jones, J.H., Oxford University Press, New York, NY.

Sweby, P.K., 1984. High resolution schemes using flux limiters for hyperbolic conservation laws, *SIAM J. Numer. Anal.,* **21**(5), 995–1011.

Sweby, P.K. & Baines, M.J., 1981. Convergence of Roe's scheme for the general non-linear scalar wave equation, Numerical Analysis Report, Reading University.

Tonks, W.B. & Melosh, H.J., 1992. Core formation by giant impacts, *Icarus,* **100**(2), 326–346.

Tonks, W.B. & Melosh, H.J., 1993. Magma ocean formation due to giant impacts, *J. geophys. Res.,* **98**(E3), 5319–5333.

Urakawa, S., Kato, M. & Kumazawa, M., 1987. Experimental study on the phase relations in the system Fe–Ni–O–S up to 15 GPa, in *High-Pressure Research in Mineral Physic,* pp. 95–111, eds Manghnani, M.H. & Syono, Y., TERRAPUB, Tokyo/American Geophysical Union, Washington, DC.

van Leer, B., 1977. Towards the ultimate conservative difference scheme. IV. A new approach to numerical convection, *J. Comp. Phys.,* **23**(3), 276–299.

von Bargen, N. & Waff, H.S., 1986. Permeabilities, interfacial areas and curvatures of partially molten systems: results of numerical computation of equilibrium microstructures, *J. geophys. Res.,* **91**(B9), 9261–9276.

Walter, M.J. & Tronnes, R.G., 2004. Early Earth differentiation, *Earth planet. Sci. Lett.,* **225**(3–4), 253–269.

Wetherill, G.W., 1985. Occurrence of giant impacts during the growth of the terrestrial planets, *Science,* **228**(4701), 877–879.

Wiggins, C. & Spiegelman, M., 1995. Magma migration and magmatic solitary waves in 3-D, *Geophys. Res. Lett.,* **22**(10), 1289–1292.

Yin, Q.Z., Jacobsen, S.B., Yamashita, K., Blichert-Toft, J., Télouk, P. & Albarède, F., 2002. A short timescale for terrestrial planet formation from Hf-W chronometry of meteorites, *Nature,* **418**(6901), 949–952.

Yoshino, T., Walter, M.J. & Katsura, T., 2003. Core formation in planetisimals triggered by permeable flow, *Nature,* **422,** 154–157.

Zimmerman, M.E. & Kohlstedt, D.L., 2004. Rheological properties of partially molten lherzolite, *J. Petrol.,* **45**(2), 275–298.

APPENDIX: ADVECTION SCHEMES

The advection of porosity requires an accurate, non-oscillatory numerical scheme that is conservative and has negligible numerical dissipation. The scheme should be able to handle extreme porosity variations or shocks. We briefly discuss a second order, time implicit, conservative, shock preserving, numerical scheme adapted from the so called 'total variation diminishing (TVD) flux limiting schemes' (e.g. Harten 1983; Sweby 1984; Pietrzak 1998) that we use. These TVD flux limiting schemes supplement a low (first) order scheme with the introduction of an additional flux. This additional flux is a difference between the flux of a higher order scheme and that of the low order scheme 'limited' (or 'corrected') in such a way as to ensure an oscillation free scheme (Sweby 1984).

Here we consider an advection equation without a source term in 1-D

$$\frac{\partial \xi}{\partial t} = -\frac{\partial (\xi \bar{v})}{\partial x} \equiv -\frac{\partial F}{\partial x}, \tag{A1}$$

where the flux $F = \xi \bar{v}$ is introduced; ξ stands for either ϕ or T in our numerical code.

We work on an equidistant staggered grid of spacing Δx where ξ is evaluated at centres of 1-D 'cells' $(\ldots, \xi_{i-1}, \xi_i, \xi_{i+1}, \ldots)$ and $\bar{v}$ has values at mid-points or boundaries of the cells $(\ldots, \bar{v}_{i-1/2}, \bar{v}_{i+1/2}, \ldots)$.

In order to attain the precision of second order in time, the partial derivative with respect to time is centred midway between the current time level t and the next time level $t + \Delta t$, that is,

$$\left.\frac{\partial \xi}{\partial t}\right|_i^{t+\Delta t/2} \approx \frac{\xi_i(t+\Delta t) - \xi_i(t)}{\Delta t}. \tag{A2}$$

The right-hand side of (A1) to be approximated is therefore $-\partial F/\partial x|_i^{t+\Delta t/2}$ and is calculated as average of $-\partial F/\partial x_i$ at times t and $t + \Delta t$, that is,

$$\left.\frac{\partial F}{\partial x}\right|_i^{t+\Delta t/2} \approx \frac{1}{2}\left(\left.\frac{\partial F}{\partial x}\right|_i^{t} + \left.\frac{\partial F}{\partial x}\right|_i^{t+\Delta t}\right). \tag{A3}$$

The spatial derivative of the flux F centred in the ith cell is approximated by (we omit the time indexing from now on)

$$\left.\frac{\partial F}{\partial x}\right|_i \approx \frac{1}{\Delta x}\left(F^+_{i+1/2} + F^-_{i+1/2} - F^+_{i-1/2} - F^-_{i-1/2}\right), \tag{A4}$$

where

$$F^{+/-}_{i+1/2} = v^{+/-}_{i+1/2}\xi^{+/-}_{i+1/2}. \tag{A5}$$

In these equations the superscripts indicate the advection direction,

$$v^+_{i+1/2} = \frac{1}{2}(\bar{v}_{i+1/2} + |\bar{v}_{i+1/2}|),$$
$$v^-_{i+1/2} = \frac{1}{2}(\bar{v}_{i+1/2} - |\bar{v}_{i+1/2}|), \tag{A6}$$

(therefore only one of v^+ and v^- can be different from zero at any midpoint), and

$$\xi^+_{i+1/2} = \xi_i + \frac{\lambda^+_{i+1/2}}{2}(\xi_{i+1} - \xi_i),$$
$$\xi^-_{i+1/2} = \xi_{i+1} + \frac{\lambda^-_{i+1/2}}{2}(\xi_i - \xi_{i+1}), \tag{A7}$$

where the two quantities $\lambda^{+/-}$ called 'limiters' are discussed below.

The approximation of the advection term (A4) can be therefore written as

$$\left.\frac{\partial F}{\partial x}\right|_i \approx \frac{1}{\Delta x}(a_i\xi_{i-1} + b_i\xi_i + c_i\xi_{i+1}), \tag{A8}$$

where

$$a_i = -v^+_{i-1/2}\left(1 - \frac{\lambda^+_{i-1/2}}{2}\right) - \frac{v^-_{i-1/2}\lambda^-_{i-1/2}}{2},$$
$$b_i = v^+_{i+1/2}\left(1 - \frac{\lambda^+_{i+1/2}}{2}\right) + \frac{v^-_{i+1/2}\lambda^-_{i+1/2}}{2} - \frac{v^+_{i-1/2}\lambda^+_{i-1/2}}{2} - v^-_{i-1/2}\left(1 - \frac{\lambda^-_{i-1/2}}{2}\right),$$
$$c_i = \frac{v^+_{i+1/2}\lambda^+_{i+1/2}}{2} + v^-_{i+1/2}\left(1 - \frac{\lambda^-_{i+1/2}}{2}\right). \tag{A9}$$

If all λ's are set to zero one gets the simple upwind difference scheme on a staggered grid, λ's equal to one give the centred difference scheme. A more complicated choice leads to the total variation diminishing (TVD) flux limiter schemes:

$\lambda^{+/-}_{i+1/2} = 0$ *UPWIND* scheme

$\lambda^{+/-}_{i+1/2} = 1$ *CENTRED* scheme

$\lambda^{+/-}_{i+1/2} = \mathcal{FL}(\mathcal{R}^{+/-}_{i+1/2})$ TVD flux limiter ($\mathcal{FL}$) schemes,

where $\mathcal{R}$ depends on the ratio of gradients of ξ (with the local gradient in the denominator and the gradient one cell upwind in the numerator) and of the velocities, that is (Laney 1998)

$$\mathcal{R}^+_{i+1/2} = \frac{v^+_{i-1/2}(\xi_i - \xi_{i-1})}{v^+_{i+1/2}(\xi_{i+1} - \xi_i)},$$
$$\mathcal{R}^-_{i+1/2} = \frac{v^-_{i+3/2}(\xi_{i+2} - \xi_{i+1})}{v^-_{i+1/2}(\xi_{i+1} - \xi_i)}. \tag{A10}$$

Various flux limiters can be chosen that have the properties to be non-oscillatory and to minimize the dissipation (Leveque 1996). They lead to numerical schemes close to second order centred differencing where the function is smooth, and close to stable upwind scheme near discontinuities.

Among the various flux limiters $\mathcal{FL}$ that were proposed, we tested

$$\mathcal{FL}(\mathcal{R}) = \max[0, \min(1, \mathcal{R})], \tag{A11}$$

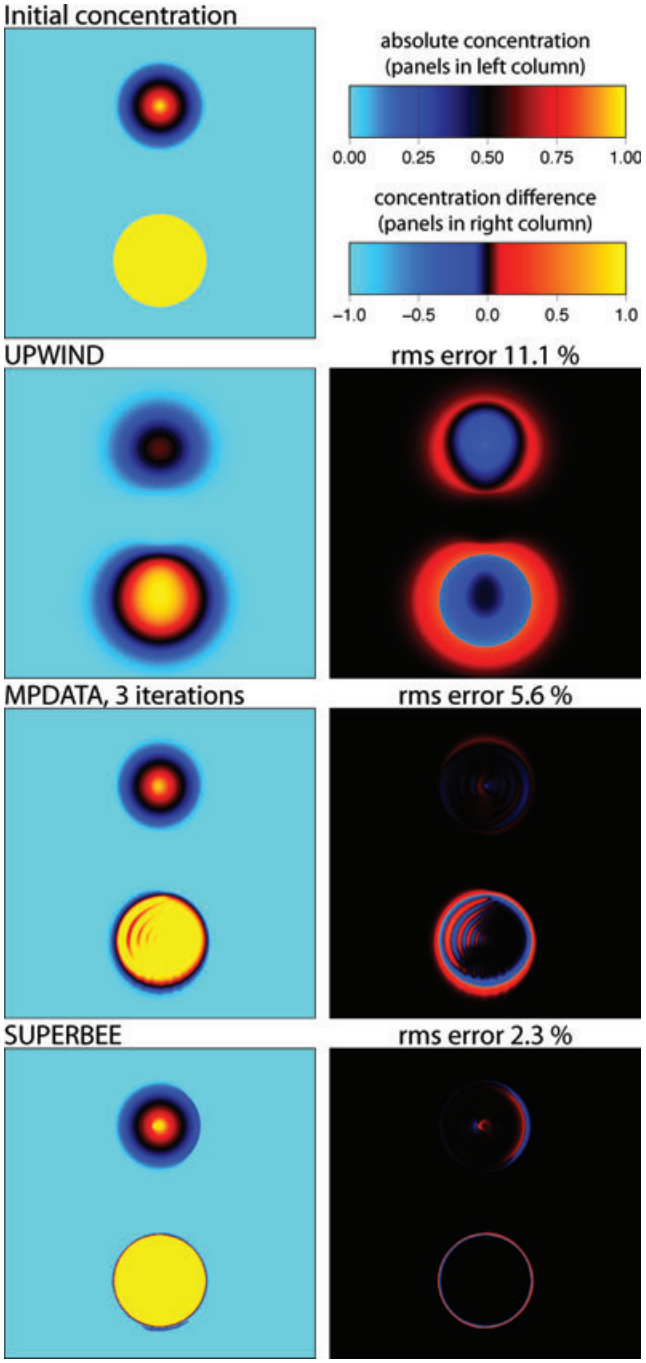

Figure A1. Test of a 2π rotation of an arbitrary concentration field shown in the top left-hand panel. The concentration after one full rotation (left-hand column) and the difference of final and initial concentration (right-hand column) are shown for the simple UPWIND scheme, the MPDATA algorithm with three iterations (Smolarkiewicz 1983), and the flux limiter SUPERBEE schemes. Calculated on a grid with 400 × 400 grid cells with the Courant number 0.4.

which gives the 'minmod' scheme (Roe's minmod transfer function; Sweby & Baines 1981) and the 'superbee' scheme (Roe's compressive transfer function; Roe 1985),

$$\mathcal{FL}(\mathcal{R}) = \max[0, \min(1, 2\mathcal{R}), \min(2, \mathcal{R})]. \tag{A12}$$

All these schemes (see also the Van Leer or MC flux limiter schemes; van Leer 1977) become centred [i.e. $\mathcal{FL}(\mathcal{R}) = 1$] when the function is linear (i.e. when $\mathcal{R} = 1$) and upwind [$\mathcal{FL}(\mathcal{R}) = 0$] near oscillations (when $\mathcal{R} \leq 0$).

The approximation (A3) requires the flux derivative $\partial F/\partial x|_i$ at both the current time level t and the next time level $t + \Delta t$. The flux derivative explicitly depends on ξ_{i-1}, ξ_i and ξ_{i+1} at the relevant time level. The numerical approximation of (A1) is therefore semi-implicit in time; in each time advancement of porosity a tridiagonal system is solved. Note that the coefficients a_i, b_i and c_i in (A8) depend on velocities and in the case of flux limiter schemes also on porosity through λ's (A9). We assume that these coefficients are constant from time t to time $t + \Delta t$, so that the eq. (A1) is solved as

$$\frac{\xi_i^{t+\Delta t} - \xi_i^t}{\Delta t} = -\frac{1}{2\Delta x}\left[a_i\left(\xi_{i-1}^t + \xi_{i-1}^{t+\mathrm{d}t}\right) + b_i\left(\xi_i^t + \xi_i^{t+\mathrm{d}t}\right) + c_i\left(\xi_{i+1}^t + \xi_{i+1}^{t+\mathrm{d}t}\right)\right]. \tag{A13}$$

If a source term S is present on the right-hand side of (A1), one needs to evaluate it at intermediate time level $t + \Delta t/2$ to keep the second-order precision in time; $S_i^{t+\Delta t/2}$ can be calculated from S at the current time level t and previous time level $t - \Delta t_{\mathrm{old}}$ from

$$S_i^{t+\Delta t/2} \approx \left(1 + \frac{\Delta t}{2\Delta t_{\mathrm{old}}}\right) S_i^t - \frac{\Delta t}{2\Delta t_{\mathrm{old}}} S_i^{t-\Delta t_{\mathrm{old}}}. \tag{A14}$$

If a diffusion term $D\partial^2\xi/\partial x^2$ is present in the eq. (A1), it can be approximated by a second order in space and time Crank–Nicolson scheme,

$$D\frac{\partial^2\xi}{\partial x^2} = \frac{D}{2\Delta x^2}\left[\left(\xi_{i-1}^t + \xi_{i-1}^{t+\mathrm{d}t}\right) - 2\left(\xi_i^t + \xi_i^{t+\mathrm{d}t}\right) + \left(\xi_{i+1}^t + \xi_{i+1}^{t+\mathrm{d}t}\right)\right]. \tag{A15}$$

The same formalism can be applied to advect the temperature and the porosity (with no diffusion term). In two dimensions they are advanced in two implicit half time steps, one in each direction (alternate direction implicit or ADI method), which on a $M \times N$ grid leads to $M + N$ tridiagonal calls in each time step.

We tested the porosity advection schemes by calculating the advection (without any source terms) of a given porosity profile by a 2-D velocity field which corresponds to a rigid body rotation. The calculation domain is a square box and the centre of rotation is in the box centre. The initial porosity is zero except in two circular regions of radius 0.15. In the bottom region the porosity is equal to 1. In the other region the porosity has a conic shape with a maximum equal to one at the centre. This initial porosity is advected by one full rotation (2π). The final porosity should therefore be identical to the initial porosity.

Fig. A1 shows the initial porosity and the resulting porosity after one full rotation for several advection schemes. The difference between the final and initial porosity is also plotted, and the root mean squared error of the final porosity is given. The simple upwind (or donor cell) scheme is highly diffusive. Much smaller error is attained when the MPDATA algorithm, here with two corrective steps (Smolarkiewicz 1983) is used. However MPDATA advection algorithm, at least in our implementation, produces ripples near porosity discontinuities. Our calculations confirm the positive definiteness of MPDATA (porosity stays above zero), but the porosity is not bound by its initial maximum value and exceeds 1. If MPDATA porosity advection were used in the two-phase numerical code, porosities above 1 would produce unphysical effects in the momentum equations. The superbee method gives the best results; we have also tested other limiters. The porosity remains bounded between the initial minimum and maximum values, which is consistent with the TVD properties of the flux limiter schemes. Our modified flux limiter schemes are semi-implicit in time. This assures their stability even for large time stepping when the Courant number is greater than one (i.e. $2\Delta t|v|/\Delta x > 1$). This is not so for the time-explicit MPDATA algorithm which becomes unstable. We use the superbee flux limiter schemes in the two-phase numerical code.